LUND UNIVERSITY
Faculty of Science

Derivation of Improved K_L^0 Response Uncertainty for use in the Jet Energy Scale Calibration at ATLAS

Per Alexander Ekman

Thesis submitted for the degree of Master of Science

Project duration: 12 months

Examination: Spring 2019

Supervised by Caterina Doglioni, Christopher Young,
and Charles William Kalderon

Department of Physics
Division of Particle Physics
June, 2019

Abstract

The Standard Model of particle physics (SM) attempts to describe the fundamental particles and how they interact with each other. This model is however incomplete, as shown by various experimental observations. ATLAS is one of the experiments currently in operation at the Large Hadron Collider, which aims to search for new physics beyond the SM. To perform these searches, many ATLAS analyses look at collimated sprays of particles, called jets, coming from proton-proton collisions. The calibration of these jets is a multi-step process that uses both simulation and data-driven methods to derive different corrections. Some of these corrections are based on a so-called response, which is a ratio between the energy of particles right after the simulated collision, and the energy of those same particles after they are simulated to interact with the detector material. The first aim of this thesis is to develop software tools that can closely investigate jet response after each step in the calibration.

Furthermore, all jet analyses are dependent on the uncertainty of the jet calibration. A major contribution to this is the uncertainty of particles called kaons (K_L^0), which is currently conservatively estimated to 20% over the entire jet transverse momentum (p_T) range. Therefore, the main aim of this thesis is to use the tools developed in order to derive a new improved K_L^0 uncertainty. This is done by looking at how the K_L^0 response changes depending on what models are used to simulate the particle interactions with the detector material.

Based on the comparison of the K_L^0 response from different interaction models, this thesis derives an improved K_L^0 response uncertainty of 20% for $p_T <$ 10 GeV, 10% for 10 $< p_T <$ 100 GeV, 2% for p_T above 100 GeV.

Contents

List of Abbreviations

SM = Standard Model
LHC = Large Hadron Collider
ATLAS = A Toroidal LHC Apparatus
CMS = Compact Muon Solenoid JES = Jet Energy Scale
MC = Monte Carlo
QCD = Quantum Chromodynamics
QED = Quantum Electrodynamics
L1 = Level-1
HLT = High-level Trigger
TLA = Trigger-object Level Analysis
HEP = High Energy Parametrized model
P = Precompound model
FTF = Fritiof string model
FTFP = Fritiof string model with Precompound model
QGS = Quark-gluon String model
QGSP = Quark-gluon String model with Precompound model
BIC = Binary Nucleon-nucleon Scattering model
LEP = Low Energy Parametrized model
BERT = Bertini Nucleon-nucleon Scattering model
CHIPS = Chiral Invariant Phase Space model
HP = High-precision neutron model
ATL = A model transition where Bertini Nucleon-nucleon Scattering model and Fritiof string model overlap in the 9-12 GeV energy range
EMY = Electromagnetic option 3

Chapter 1

Introduction

The Standard Model of particle physics (SM) attempts to describe the fundamental particles and how they interact with each other. Ever since its proposal, the SM has undergone multiple additions and improvements in order to accommodate new discoveries and more precise measurements. Despite the success of the SM describing experimental observations, there are well-known missing pieces. For example, the SM does not yet include observed phenomena such as dark matter, neutrino masses, or gravity [1]. In order to expand the SM to include new physics, both additions to the theory and observed missing pieces need further experimental verification.

Particle colliders such as the Large Hadron Collider (LHC) are necessary tools for performing these experimental verifications. At the LHC, two beams of high energy protons are accelerated in opposite directions and collided with each other, as introduced in Section 2.7. In these collisions, different interaction processes can occur, and with the SM, it is possible to predict at what rates such processes should occur. ATLAS (A Toroidal LHC Apparatus), described in Section 2.8, is one of the experiments currently in operation at the LHC which aims to test the predictions of the SM and look for new physics beyond the SM by measuring the properties of the final state particles that come out of these interaction processes. These measurements can then be used to confirm or refute theoretical predictions.

Collimated sprays of particles are often observed as a result of the collision processes. These sprays originate from the fundamental proton constituents, the quarks and gluons. As these particles propagate through the detector, they interact with its material and deposit their energy in different ways. Some of these interactions make the original particles produce further cascades that deposit energy in the detector material, and this allows us to measure the energy of the initial particles. By grouping multiple such energy deposits together using algorithms, we can reconstruct physics objects called jets, which are discussed further in Section 3. These jets are important tools which allow us to relate our experimental observations in data to the initial final state quarks and gluons of the collision process.

Many analyses at the ATLAS experiment involve jets, and it is crucial that the measured energies of these jets are calibrated precisely in order to properly compare the ATLAS measurements to the predictions of the SM. The jet energy scale (JES) calibration is a chain of multiple steps, where each step corrects the measured jet energy for different detector effects and brings the jet energy measured in the detector to the energy

of the original particle shower. The details of the JES calibration are covered in Section 3.2.

One of the steps of the calibration is called the absolute JES. For this calibration step, proton-proton collisions are simulated through Monte Carlo (MC) and the resulting showers of particles are called *truth* particles, which can be grouped into *truth jet*. Further MC simulation is applied to the truth particles in order to recreate their energy deposits in the detector, which are then grouped into reconstructed jets. Finally, the energy ratio of the reconstructed and truth jet, called a response, gives a correction factor which brings a reconstructed jet to the energy of the original particle shower.

Since jets contain many different particles, the uncertainty of the JES calibration is dependent on the properties of all these different particles. The uncertainty associated with the K_L^0 hadron is one of the dominant contributions to the JES calibration uncertainty, as K_L^0 are abundant in jets and cannot easily be studied in test-beams.

The aim of this thesis is to develop the tools necessary to investigate the different responses in the JES calibration and use these tools to specifically investigate the K_L^0 uncertainty contribution. The tools developed will also be used in the future to verify that the calibration steps in the JES calibration do not introduce any unwanted effects in the analyses using it.

Chapter 2

Theory and Experimental Background

This chapter describes the basic theory of particle physics, its shortcomings and some of the experimental methods and tools used today to improve the theory. This section also serves as an introduction to the basic concepts needed for understanding the procedure and motivation of the work done in this thesis.

2.1 The Standard Model (SM)

The Standard Model (SM) is a theoretical model of particle physics which aims to describe the elementary particles and their interactions with each other [3]. As visualized in Figure 2.1, the SM currently includes 12 matter particles, as well as their antiparticles, and describes their interactions using three fundamental forces through four force mediators. The fourth fundamental force, gravity, has not yet been included in the model. The particles are divided into different groups, the matter particles of half-integer spin called fermions, the integer spin particles which mediate the three fundamental forces called gauge bosons, and the Higgs boson which is a scalar boson with spin 0 and plays an important role for some of the other particles' masses.

The 12 fermions are divided into groups depending on their characteristics. As shown in Figure 2.1, the leptons are further split into three generations, with two leptons in each generation. The electron, muon, and tau all have an electric charge and interact via the electromagnetic and weak force. The neutrinos have no electric charge and only interact via the weak force. The quarks are also split into three generations, each including two quarks separated by one integer value of electric charge. The quarks are also the only fermions to have color charge. The antiparticle associated to each fermion has the same mass and spin but opposite charges.

Fermions can interact with each other via a mediator of an associated force, where each force has different properties. The electromagnetic force couples to electrically charged particles and its mediator is the massless photon. The electromagnetic force is stronger than the weak force but weaker than the strong force. The weak force is carried by the $W^{+/-}$ and Z bosons which are massive particles that couple to all species of fermions and the Higgs. Due to its electric charge the $W^{+/-}$ also couples to the photon. The strong force is mediated by the gluon, which couples to particles with color charge, and like the

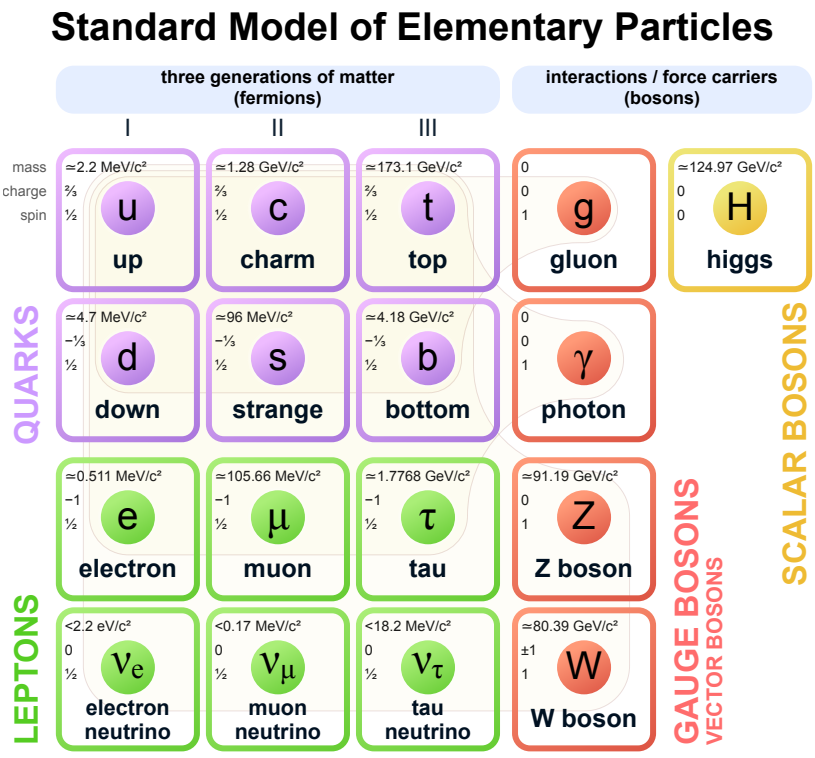

Figure 2.1: A visual representation of the 4 leptons, 4 quarks, 4 force carriers, the Higgs boson, and how they are grouped depending on their characteristics in the Standard Model [2].

photon it is also massless. Unlike the photon, it carries a non-zero color charge which makes it self-interacting, and this self-interaction gives rise to the phenomena discussed in Section 2.2.

The most recently discovered particle is the Higgs boson, which is an excitation of the Higgs field. The $W^{+/-}$ and Z obtain their mass from what is called the Higgs mechanism, and all the fermions interact with the Higgs boson via a strength proportional to their mass, except the neutrinos. Since there are no observed so-called *right-handed* neutrinos or *left-handed* anti-neutrinos, these aren't included in the SM and the neutrino masses do not appear in the model as for the other fermions [4].

2.2 Quantum Chromodynamics (QCD)

In the SM the electromagnetic force is described by Quantum Electrodynamics (QED) and the strong force is described by Quantum Chromodynamics (QCD). Figure 2.2 shows an example diagram of quark-quark scattering by gluon exchange. Both the strong force and the electromagnetic force are mediated by massless spin-1 bosons that couple to their associated charges, and there are diagrams similar to that of Figure 2.2 in QED. The crucial difference between QCD and QED is the self-interaction of gluons, which gives rise to an asymptotically decreasing interaction strength as a function of momentum transfer. At high and low momentum transfer, we observe two different phenomena.

Firstly, the strong force is weak at very high momentum transfers (short distances), in the asymptotic freedom regime, which allows the quarks to be quasi-free particles instead of bound while within the proton and other hadrons. Secondly, the strong force is very strong at low momentum transfer (larger distances), in the color confinement regime. Color confinement refers to the fact that quarks and gluons are never observed as free particles and all observed bound states have zero color charge. Color confinement lies at the core of the hadronization process for quarks and gluons which creates the jets observed at the Large Hadron Collider (LHC), discussed in Section 3 [3, 5].

2.3 Four-vectors

In order to study the particle interactions of the SM, we need a way to represent the particles mathematically. One of these representations is in the form of a so-called four-vector. From Einstein's postulation that the speed of light in a vacuum is the same in all inertial frames, it follows that the space-time coordinates in two different inertial frames are related by the Lorentz transformations [5]. Because the inertial frame of interactions in particle collisions at the LHC are not always stationary with respect to the inertial frame of the observer, it is beneficial to express observable quantities in a form that can be applied to all inertial frames. Such a form is called a Lorentz-invariant form, and for a relativistic particle of mass m we identify its energy, E, and momentum, $\vec{p}$, as [5]:

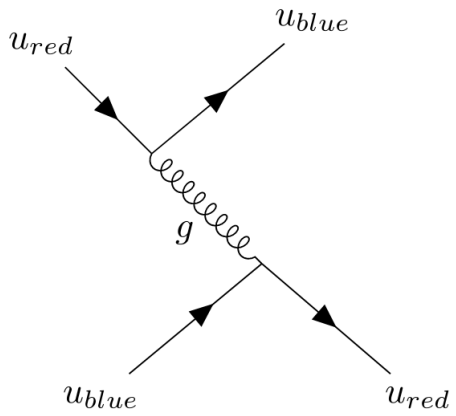

Figure 2.2: Diagram showing quark-quark scattering through gluon exchange, one of the more common processes in the proton-proton collisions at the Large Hadron Collider.

$$E = \frac{1}{\sqrt{1-\frac{\vec{v}^2}{c^2}}}mc^2 \quad , \quad \vec{p} = \frac{1}{\sqrt{1-\frac{\vec{v}^2}{c^2}}}m\vec{v} \tag{2.1}$$

It can be shown that energy and momentum defined this way can form a so-called covariant four-vector, also called four-momentum, p^μ [5]:

$$p^\mu = (E, p_x, p_y, p_z) \tag{2.2}$$

This object contains the particle's spatial momentum and energy, and from the properties of four-vectors, the magnitude of this four-momentum is defined as $p^\mu p_\mu = E^2 - \vec{p}^2$, which is a Lorentz-invariant quantity independent of the inertial frame. From Equation (2.1) it is seen that a particle in its own inertial frame has four-momentum $p^\mu = (m, 0, 0, 0)$ with magnitude $p^\mu p_\mu = m^2$. Since this scalar product is Lorentz-invariant, this relation is true in any inertial frame, giving the Lorentz-invariant relation:

$$p^\mu p_\mu = E^2 - \vec{p}^2 = m^2 \tag{2.3}$$

Where E and $\vec{p}$ are measurable quantities by our detectors. This also holds for a system of particles, in the case of an unstable particle of mass, m, decaying into decay products A and B, we get the so-called invariant mass of the decaying particle using the following relation [5]:

$$(p_A + p_B)^\mu (p_A + p_B)_\mu = m^2 \tag{2.4}$$

Since the invariant mass is a measure of particle mass, independent of the inertial frame, this is an important experimental observable used in the search e.g. for the Higgs boson and other new particle searches at ATLAS, as will be discussed in more detail in Section 2.6.

2.4 $\mathbf{K_L^0}$

The K^0 and $\bar{K^0}$ are the bound states of an up and anti-strange quark, and an anti-up and strange quark respectively. Through the weak interaction, the K^0 and $\bar{K^0}$ can mix, meaning that a kaon produced as a K^0 develops a $\bar{K^0}$ component and vice versa. As a consequence, neutral kaons propagate as linear combinations of K^0 and $\bar{K^0}$ described by the states [5]:

$$|K_1\rangle = \frac{|K^0\rangle + |\bar{K^0}\rangle}{\sqrt{2}} \ , \ |K_2\rangle = \frac{|K^0\rangle - |\bar{K^0}\rangle}{\sqrt{2}}$$

To investigate the properties of K_1 and K_2, let us consider the two symmetry operators parity ($\hat{P}$) and charge conjugation ($\hat{C}$). A system described by a quantum mechanical wave function, $\psi(\vec{x})$, transformed by the parity operation, has all coordinates inverted through its origin. A system is then invariant under parity if $\hat{P}\psi(\vec{x}) = \pm\psi(\vec{x})$ [4]. It can be shown that parity is conserved in electromagnetic and strong interactions, but experimental observations have shown that weak interactions do not conserve parity [6, 5]. The charge conjugation operator replaces a particle by its antiparticle. If an interaction is invariant under charge conjugation it means that if a particle can undergo a certain interaction, so can its antiparticle.[1]

The K^0, $\bar{K^0}$, and consequently their linear combinations K_1 and K_2, are not C eigenstates, but are P and CP eigenstates of the neutral kaon system with the following CP eigenvalues [3]:

$$\hat{CP}\,|K_1\rangle = \frac{|\bar{K^0}\rangle + |K^0\rangle}{\sqrt{2}} = |K_1\rangle \ , \ \hat{CP}\,|K_2\rangle = \frac{|\bar{K^0}\rangle - |K^0\rangle}{\sqrt{2}} = -\,|K_2\rangle$$

The CP eigenvalues for a system of two pions is +1, and -1 for a system of three pions [5, 3]. If CP was conserved in weak interactions, the kaon hadronic decays would exclusively be $K_1 \to \pi\pi$ and $K_2 \to \pi\pi\pi$, and due to the three-body decay of K_2 its lifetime would be longer than that of K_1.

In neutral kaon beam experiments, two states of neutral kaons are observed with very similar masses, different hadronic decays, and different lifetimes. The short-lived $\mathrm{K_S^0}$ with a lifetime of $0.8954 \cdot 10^{-10}$ s, decays predominantly to two pions. The long-lived $\mathrm{K_L^0}$ with a

[1] As mentioned in Section 2.1, there are no observed left-handed anti-neutrinos, meaning that interactions involving left-handed neutrinos do not occur for left-handed anti-neutrinos. Therefore, the weak interaction is not invariant under charge conjugation.

lifetime of $5.116 \cdot 10^{-8}$ s, decays predominantly to three pions [7]. As a close approximation we therefore identify the states $K_S^0 \approx K_1$ and $K_L^0 \approx K_2$. If CP symmetry was not violated, K_S^0 would decay exclusively to two pions, K_L^0 exclusively to three pions, and we could directly correlate them to their CP eigenstates. However, experiments have shown that K_S^0 and K_L^0 have a small but significant probability to undergo the decays $K_S^0 \to \pi\pi\pi$ and $K_L^0 \to \pi\pi$, decays which do not conserve CP, called CP violation [5]. It is, however, possible to incorporate CP violation into the SM, the details of which is beyond the scope of this thesis [3].

Apart from describing the neutral kaon hadronic decays, the incorporation of CP violation in the SM also describes the cause of the difference in rates of the K_L^0 semi-leptonic decays $K_L^0 \to \pi^- e^+ \nu_e$ and $K_L^0 \to \pi^+ e^- \bar{\nu}_e$. Where the number of observed decays involving an anti-electron is found to be 0.66% larger than the decays involving an electron [5]. The explanation of this matter-antimatter asymmetry is however not enough to explain the asymmetry observed in the universe today [5]. Answering the question of why the observable large-scale structures of the universe are only made of matter, is only one of the problems with the SM.

2.5 Some Problems with the Standard Model

In a simple model of the big bang there would have been equal amounts of matter and antimatter created. However, observations of cosmic rays show that they are mainly composed of matter, nor are there any observations of electromagnetic radiation to support large scale annihilation of matter and antimatter. The lack of antimatter in the universe is a serious problem for this simple big bang model and the SM. As discussed in Section 2.4, CP violation in the SM explains some matter-antimatter asymmetries, but the origin and size of these CP violations are not enough to explain the observed matter-antimatter asymmetry of the universe [3]. There are other problems like this with the SM, where the major problems can be split into two categories: observations that are not explained in the theory, and aesthetic problems of the theory [8].

Apart from the observed matter-antimatter asymmetry of the universe, astronomical observations have by observing different objects with different methods confirmed the existence of dark matter [9]. Dark matter is observed as something that adds mass to objects like galaxies, mass which cannot be accounted for by other observable objects. Dark matter may be explained by a new type of massive particle which does not reflect, absorb, or emit light, a phenomenon which is also not included in the SM [10]. As mentioned in Section 2.1, neutrino masses do not appear in the SM as for the other fermions. This is problematic because experiments such as the Super-Kamiokande neutrino detector has shown evidence for neutrino masses, explained by a mechanism called *neutrino oscillations*, which is not yet included in the SM [11, 12]. Another physics phenomena not included is the force of gravity. Since the aim of the SM is to explain how fundamental particles interact, it is problematic that it does not include the fourth fundamental force of gravity. Even though gravity is too weak to be considered at the scale of particle interactions, the SM fails to explain why it is so much weaker than the other three forces [10].

For the second category of problems, there are aesthetic problems with the SM. These are details in the theory which are consistent with experimental observations but lack

the elegant mechanisms which we are, to our standards, to some degree expecting [8]. One of these is the so-called hierarchy problem. In the SM, the Higgs boson obtains a large contribution to its mass from what is called *quantum loop corrections*. This is not a problem in itself, but at very large energy scales these corrections contribute to a very large Higgs mass. To keep the Higgs mass at the observed electroweak scale of 10^2 GeV, new contributions to the Higgs mass are added and fine-tuned in order to cancel the other contributions [5]. This fine-tuning of the quantum loop corrections is considered an un-aesthetic solution to the problem, and theoretical extensions of the SM (such as supersymmetry, where each SM particle has a supersymmetric partner particle) are proposed in order to, among other things, remove this fine-tuning [5].

2.6 Finding New Physics

There are many searches for new physics to expand and improve the SM, an example of which are the many searches for new particles at the ATLAS and the Compact Muon Solenoid (CMS) experiments. In proton-proton collisions at the LHC, SM and non-SM particles can be created. If these particles are unstable and decay too quickly to be observed directly, we can study them by detecting and measuring their decay products [13]. Such observed particles are called resonances. Shown as a mediator in Figure 2.3, these resonances are formed as intermediate steps between the initial particle interaction and the final state products. By measuring the properties of the decay products it is possible to calculate the invariant mass of the resonance, as discussed in Section 2.3.

The Higgs boson was, among other particles, discovered in such a way. From its decay into two photons, measurements of two-photon events were used to form a distribution of the di-photon invariant mass, as shown in Figure 2.4. A fit to the data, where the fit function does not accommodate local excesses, is used to estimate the SM background in absence of the Higgs boson. As seen in the bottom of Figure 2.4, the difference between the data and the background fit then shows a significant excess at the invariant mass of 126.5 GeV, the mass of the Higgs boson [14].

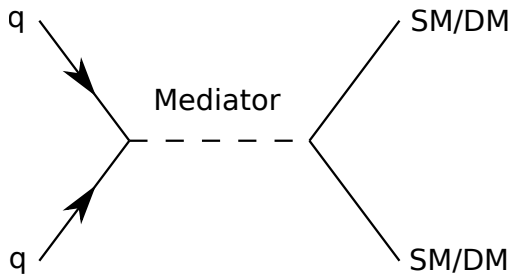

Figure 2.3: A possible diagram showing the production and decay of a proposed dark matter mediator decaying into either dark matter or Standard Model particles

It is in the same way possible to search for new resonant particles. As shown in Figure 2.3, we can postulate a resonant particle, called a mediator, which in this example couples to both SM and dark matter particles. Dark matter itself does not interact with the ATLAS detector, but if this mediator decays into SM particles, its invariant mass can be determined in a similar way as it was done for the Higgs. The properties and decays of such a mediator can then be studied further in order to investigate potential dark matter production. Since no new resonant particle has been observed yet, we can assume that events where this mediator decays into detectable SM particles are very rare and do not occur very often in the

proton-proton collisions at the LHC. This is why many analyses benefit from obtaining as many events as possible.

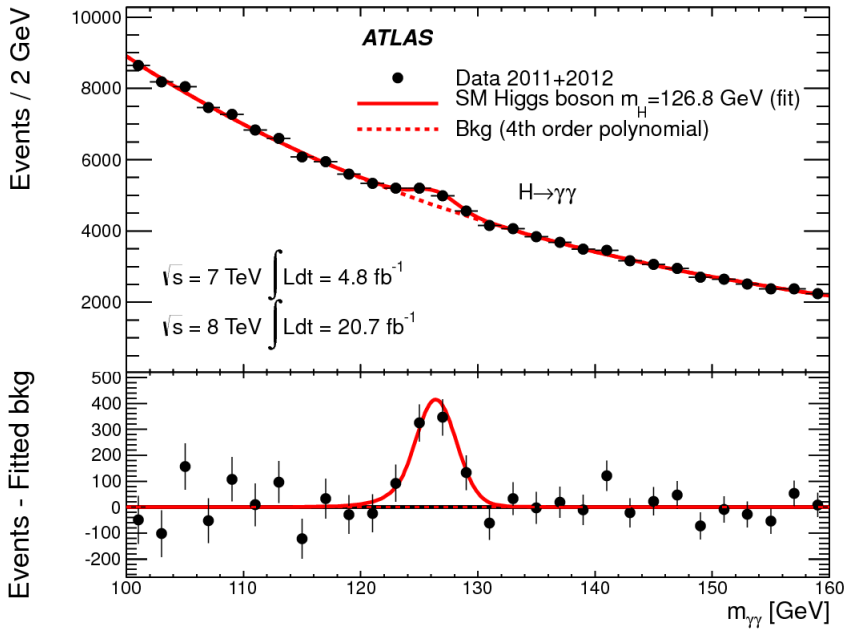

Figure 2.4: Invariant mass distribution from Higgs diphoton event candidates combined for the $\sqrt{s} = 7$ and 8 TeV data. The difference between the fitted Standard Model background and the data is shown in the lower panel indicating a Higgs mass of 126.5 GeV [15].

2.7 LHC

The LHC is an accelerator which accelerates particles in two counter-rotating beams and collides them at four points where detectors are located. Due to the technique used for accelerating the particles, protons at the LHC end up in bunches rather than a continuous current. Because of these bunches, at the point of collision, there are multiple interactions along the beam line and in its transverse plane. This means that in a collision of two bunches, called a bunch crossing, multiple interactions occur with a spread around the center of the detector. This leads to an uncertainty in the spatial position of the interactions, and it also means that particles from different interactions can interfere with each other. Such interference is referred to as pile-up, and there are two types of pile-up. Out-of-time pile-up are effects in the detector from previous and subsequent bunch crossings. In-time pile-up are effects from other interactions in the same bunch crossing. Pile-up is often parameterized in terms of the average number of interactions per bunch crossing, $< \mu >$, and the number of proton-proton interactions (primary vertices), N_{PV}. How we correct for the effects from off-center interactions and pile-up is discussed further in Section 3.2.1 and 3.2.2 respectively.

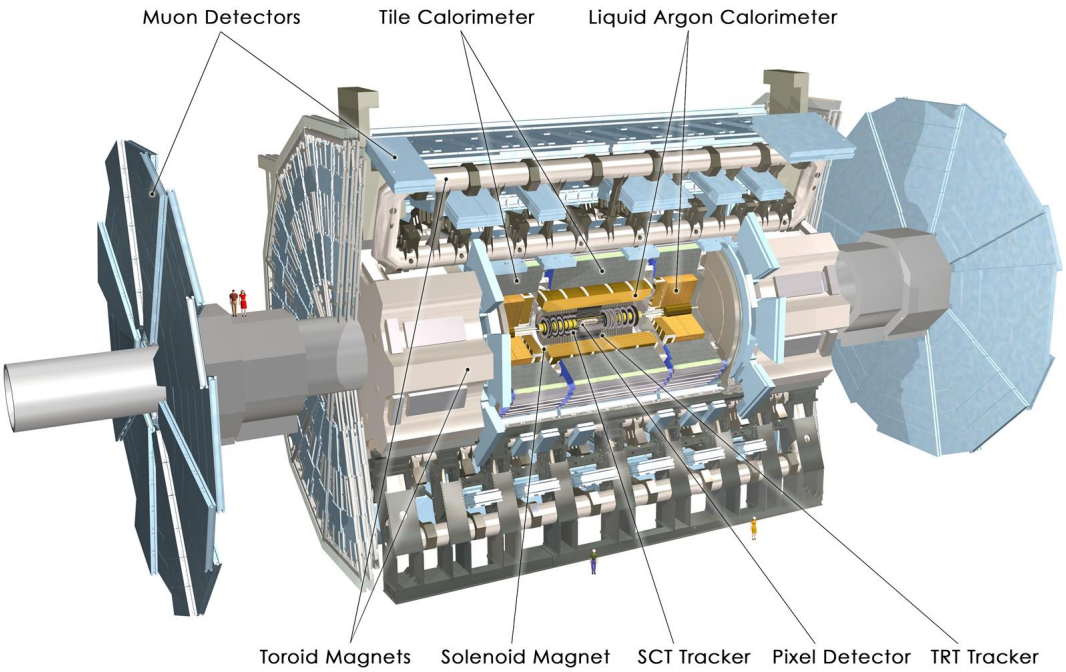

Figure 2.5: Computer generated image of the whole ATLAS detector with labels of the different detector components [16]

2.8 ATLAS

As seen in Figure 2.5, the ATLAS detector is cylindrical with different detector layers placed concentrically. To record the trajectory of particles there is a need to define a coordinate system of the detector. In an ordinary Cartesian coordinate system the ATLAS detector is oriented such that the x-axis points to the center of the LHC, the y-axis points vertically upwards, and the z-axis is in the beam direction. Since the transverse momentum of the particles before collision is close to zero, this means that any transverse momentum, p_T, observed from the final state particles can be associated with the particle interaction itself, excluding leftover momentum in either beam direction. p_T is an important quantity in collider physics which is used extensively in this thesis. Because of the cylindrical shape of ATLAS, it is beneficial to use a cylindrical coordinate system for the particles inside it. As shown in Figure 2.6, for the cylindrical coordinates the z-axis is still in the beam direction, ϕ is the azimuthal angle measured from the x-axis, and θ is the polar angle measured from the positive z-axis.

The polar angle θ is often replaced by the pseudorapidity η defined by equation (2.5)

$$\eta \equiv -\ln\left[\tan\left(\frac{\theta}{2}\right)\right] \tag{2.5}$$

Pseudorapidity is preferred over θ because a difference in rapidity between two particles is Lorentz invariant under boost along the z-axis [5]. A representation of how the pseudorapidity is related to the polar angle θ is shown in Figure 2.7.

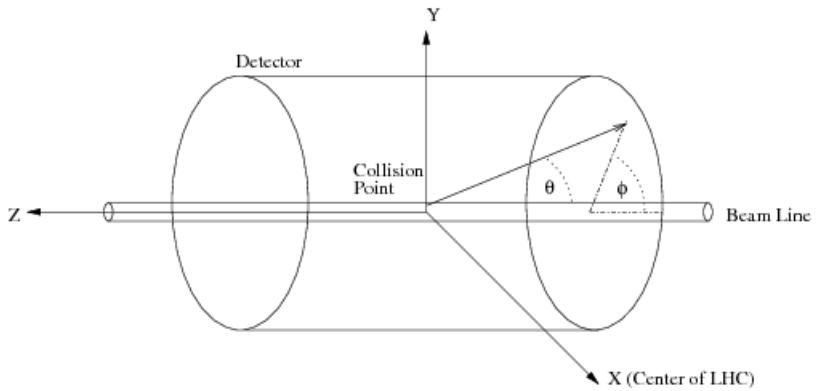

Figure 2.6: The cylindrical and Cartesian coordinates of the ATLAS detector in relation to the Large Hadron Collider and beam [17].

The detector contains four major components: inner detector, electromagnetic calorimeter, hadronic calorimeter, and muon spectrometer. Each component serves a different purpose, as ATLAS is a so-called general-purpose particle detector. In the center of the inner detector, closest to the particle collisions, is the pixel detector. It consists of approximately 1700 identical silicone pixel modules which correspond to a total of $8 \cdot 10^7$ pixels [19]. Surrounding the pixel detector is the Semi-Conductor Tracker. It is similar to the pixel detector but uses narrow strips rather than small pixels in order to cover its larger area [20]. Lastly, the outer shell of the inner detector is the Transition Radiation Tracker. To keep the costs low and cover the large remaining volume, it uses 298 000 straws acting as drift tubes to detect charged particles [21]. Surrounding the whole inner detector is a solenoid magnet which provides a 2 T axial magnetic field. When charged particles move through the magnetic field, the Lorentz force bends their trajectory. Because of the high density of detector elements sensitive to charged particles in the inner detector, it is possible to reconstruct the trajectories of individual charged particles as visualized in Figure 2.8. This trajectory, together with information from the other parts of the detector, is crucial for identifying the particle species and measure the particle's momentum.

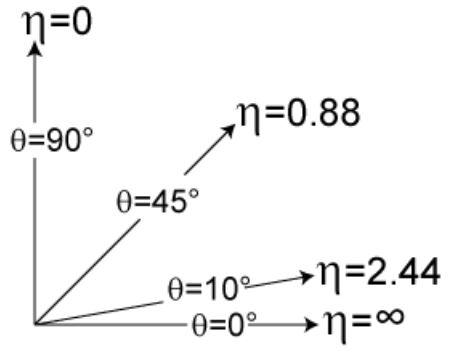

Figure 2.7: A visualization of the relationship between pseudorapidity, η, and the polar angle θ [18].

After a particle has passed through the inner detector, where the tracking is done, the energy of the particle will be measured by absorbing it. This is done by the two sampling calorimeters: the inner electromagnetic calorimeter and outer hadronic calorimeter. They absorb energy from the particles in high-density metal and periodically sample the resulting particle shower in order to infer the energy of the initial particle. Details of particle interactions with the detector are covered in Chapter 4.

The electromagnetic calorimeter uses lead and stainless steel absorbers to develop the showers from which secondary particles create ionization of the liquid argon. An inductive

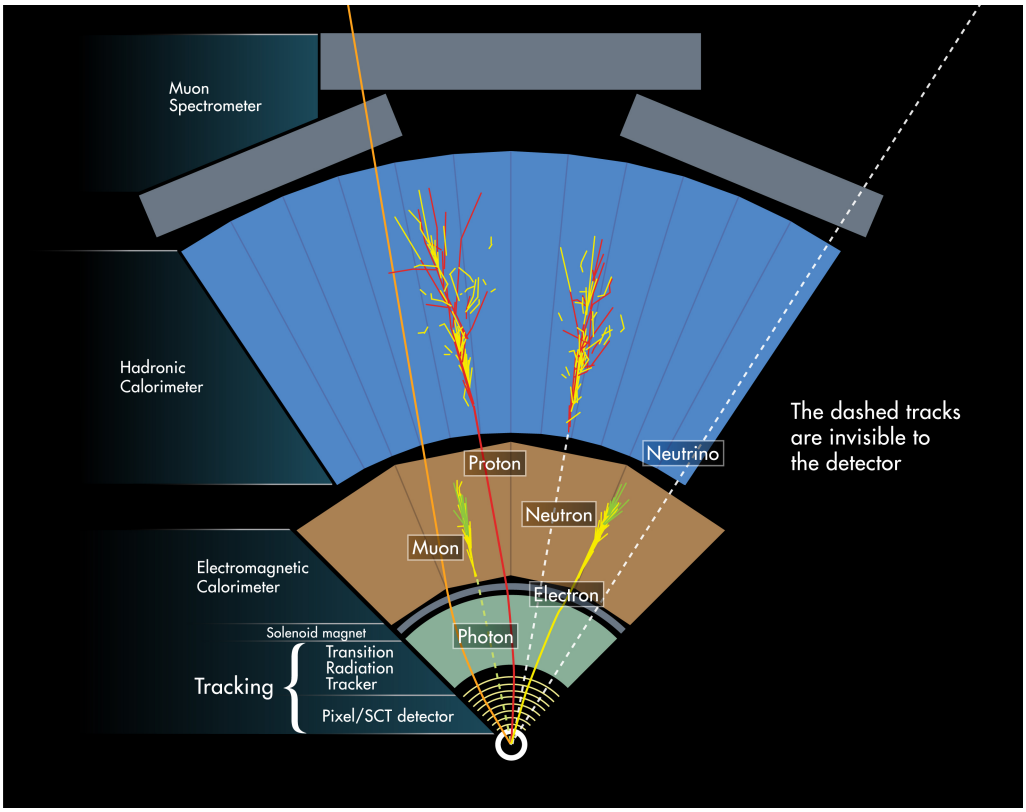

Figure 2.8: A cross-sectional graphic of the ATLAS detector with the different detector components in a concentric formation. It further visualizes how the different detector layers are used together to identify different particles [25].

signal from the ionization is then registered by copper electrodes which give positional and amplitude information about the energy deposit. The electromagnetic calorimeter has good precision in measuring the energy absorbed as well as the spatial position of the absorption [22]. Together with the tracking, the properties of the electromagnetic calorimeter help us identify particles by how they interact electromagnetically as visualized in Figure 2.8.

The hadronic calorimeter uses stainless steel absorbers and scintillating tiles to sample the energy deposit. It mainly measures the energy from particles that pass through the electromagnetic calorimeter and finally interacts via the strong force in the hadronic calorimeter, as visualized in Figure 2.8. Because of the large distances needed for hadronic interactions, it covers a much larger volume, and therefore uses cheaper material and is less precise in its energy and spatial measurements [22].

Both of these calorimeters are so-called non-compensating calorimeters. This means that they respond differently to energy deposits by electromagnetic interactions and hadronic interactions [23]. Detector effects such as this is one of the reasons that measured objects at ATLAS have to be calibrated for different detector effects.

Lastly, the muon spectrometer forms the outermost layer of the ATLAS detector. Muons produced at the LHC penetrate the other layers with ease and are therefore difficult to measure. The muon spectrometer uses drift tubes to measure the momenta of these muons [24].

2.8.1 Data Processing at ATLAS

The LHC collides bunches of protons at a rate of roughly 40 MHz, where each bunch crossing contains multiple proton-proton interaction events. At this high rate, it is not possible for ATLAS to process and store all the events, as each event is roughly 1 MB in size. Deciding which events are worth processing and keeping in long term storage is handled by the ATLAS trigger and data acquisition system [26]. The trigger system is a two-stage system used to select events for analysis and final long term storage. The Level-1 (L1) trigger is the first stage and is tasked with picking interesting events, and bringing the initial 40 MHz bunch crossing rate down to an interaction event rate of 75 kHz. The L1 trigger uses a list of criteria, which determine if an event is to be saved or not. These criteria could be for example that a calorimeter energy deposit has a transverse momentum, p_T, above a certain threshold, that there are above a certain number of electrons/photons in the event, etc. If an event does not pass the criteria, the event information is discarded. The readout from accepted events is passed to the High Level Trigger (HLT).

The HLT consists of software-based triggers, which use more refined event data and similar reconstruction algorithms as used in the final analyses after the data is recorded, called offline analysis. This means that the HLT can make much more complex decisions. The HLT selection brings the final rate of proton-proton collisions down to roughly 200 Hz [27]. These events then enter long term storage and are used for offline analysis.

As the number of interactions delivered by the LHC increases, due to hardware and software restrictions, the triggers have to use stricter criteria and discard a larger percentage of the events. This is not optimal as the discarded events could be events with information of new physics. However, data recording techniques such as Trigger-object Level Analysis (TLA) can circumvent these restrictions by using events of a smaller size, as discussed in Section 5.2. Because of the resulting larger amount of analyzed events, TLA is a useful tool looking for rare events such as the decay of new resonant particles, as covered in section 2.6.

Chapter 3

Jets

In the proton-proton collisions at the Large Hadron Collider (LHC), strong force processes such as that in Figure 2.2 dominate the interactions. Due to their abundance, one of the most commonly occurring observable objects at ATLAS are the collimated particle showers resulting from these final-state quarks and gluons. As the particles interact with different parts of the detector they deposit their energy which is then measured. The measurements of these deposits are then used in algorithms which reconstruct so-called jets. When properly calibrated, jets are important tools which allow us to relate our measurements to the final state quarks and gluons of the collision process. This chapter presents how these jets are reconstructed both in data and in simulation, as well as the calibration done in order to correct the jet energy for different detector effects.

3.1 Jet Reconstruction

As mentioned earlier, processes like the one shown in Figure 2.2 are common at proton-proton collisions at the LHC. Before the collision, the quarks are initially bound in the proton, but because of the high momentum transfer through the gluon, the constituents of the proton are separated at high energies. As introduced in Section 2.2, due to color confinement, these quarks and gluons cannot be free particles. They undergo a process called hadronization, where the energy stored in the color field between them is large enough to produce new quark-antiquark pairs. This process continues for the newly created quark pairs until all quark pairs have low enough energy to form colorless hadrons such as pions, kaons, etc. This hadronization process is visualized in Figure 3.1 [5].

Because of the large momentum of the initial quark or gluon, the hadronization leads to a collimated spray of particles. As these particles propagate through the ATLAS detector they leave signals in the tracker and calorimeters, and using so-called jet algorithms, the four-vectors of either particles or of the detector signals can be combined to form a reconstructed object called a jet.

This section will describe how jets are reconstructed using a jet algorithm for data as well as for simulation. The reconstructed jets are at the so-called EM-scale, meaning that the energy has been correctly measured for particles depositing their energy through electromagnetic interactions only [23].

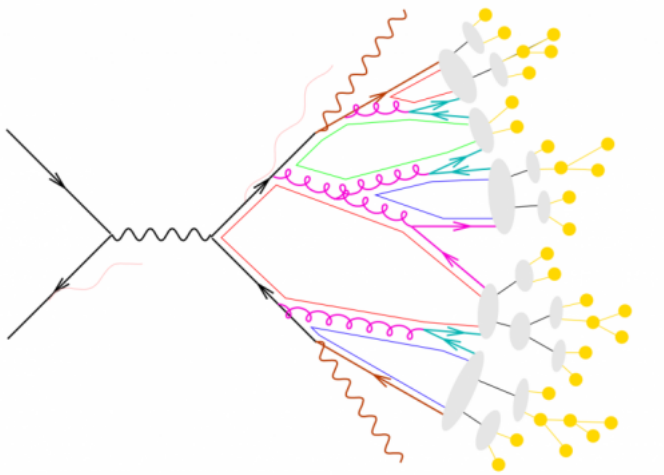

Figure 3.1: A visual interpretation of the hadronization process of quarks and gluons [28].

3.1.1 Reconstructing Jets in Data

The first step of reconstructing a jet in data taken at the ATLAS detector is done by grouping cells of the calorimeter into so-called topo-clusters [29]. Topo-clusters are formed using a growing-volume algorithm, which starts from a cell with a signal-to-noise ratio above a certain threshold and then grows to include neighboring cells with lower energies. After this algorithm, the individual cells have been grouped into topo-clusters as shown in Figure 3.2. The total energy of a topo-cluster is obtained by a vector sum of the cell energies included in the cluster. Meanwhile, the topo-clusters direction is determined by a straight line from the center of the detector to a signal-weighted barycenter of the clustered cells [29].

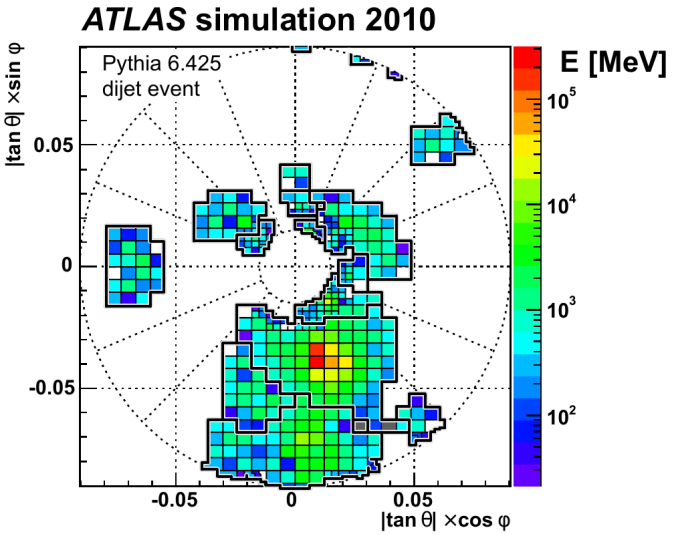

Figure 3.2: The final topo-clusters formed after the growing volume algorithm has expanded out from seeding cells, which have a signal-to-noise ratio above a certain threshold, to include lower energy cells [29].

The direction and energy of the multiple topo-clusters in an event make up the four-vectors which serve as input to the jet algorithm. The goal of the jet algorithm is to take these four vectors and reconstruct jets associated to them. The general functionality of a jet algorithm can be explained by considering an event with a few high p_T four-vectors and many low p_T four-vectors. The algorithm works in such a way that the low p_T four-vectors tend to be clustered to high p_T ones before clustering with themselves. If two high p_T four-vectors are close to each other, their shapes will not be conical. The main algorithm used to reconstruct jets in ATLAS is the anti-k_T algorithm [30]. As seen in Figure 3.3, the boundaries between overlapping jets are different depending on the p_T

of the four vectors associated with the jet. This is a feature of the jet algorithm which makes sure that jets are reconstructed consistently from event to event, independent on small energy fluctuations such as pile-up, as introduced in Section 2.8.

3.1.2 Reconstructing Jets and Truth Jets in Simulation

For jets in simulation, the collision process of initial and final state particles originate from simulation using the Pythia event generator [31]. The final state particles then undergo a simulated hadronization process resulting in collimated showers of particles. Each particle in such a shower has an associated four-vector. The so-called truth jets are formed by taking these four-vectors at this stage as inputs to the jet algorithm.

Jets are reconstructed in simulation by taking the same post-hadronization particles as used for the truth jet, but using Geant4 [32] simulations of how they propagate through and deposit energy in the material of the ATLAS detector. From these simulated energy deposits, topo-clusters are created, and their four-vectors used as inputs to the jet algorithm which will then reconstruct the simulated reconstructed jets.

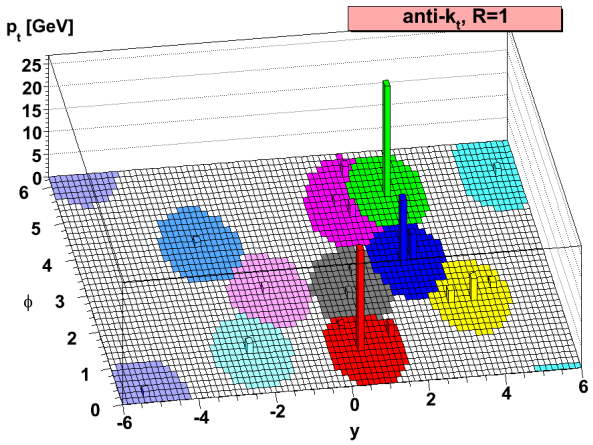

Figure 3.3: The final reconstructed jet output of the jet algorithm anti-kt [30] after using four-vectors from simulated topo-clusters as inputs [30].

3.2 Jet Energy Scale (JES) Calibration

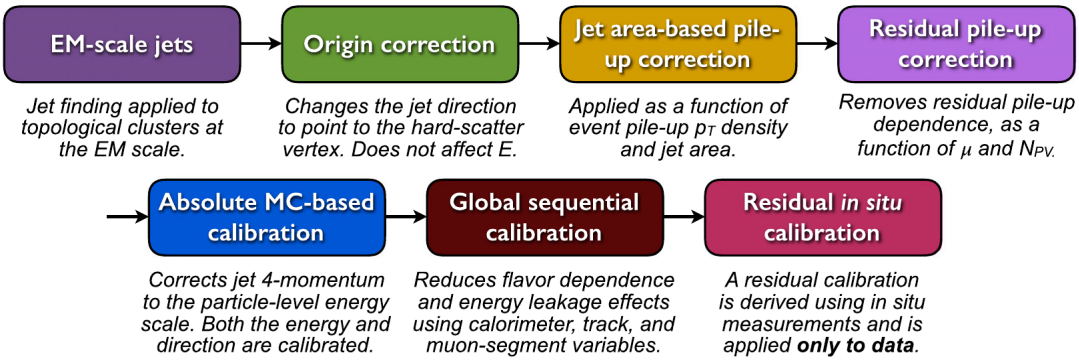

Figure 3.4: The order and description of the calibration steps used in the Jet Energy Scale (JES) calibration, which is applied to jets at the EM-scale [33].

Since particles within a jet undergo a variety of interactions and energy losses when traversing the detector, reconstructed jets need to be calibrated so that their original

energy (called the jet energy scale, or JES) can be restored.

This section presents the 2015 calibration scheme that corrects EM-scale calorimeter jets to their full jet energy scale. This calibration consists of multiple steps which correct for different effects, described below. The order of the steps in the calibration is shown in Figure 3.4.

3.2.1 Origin Correction

As mentioned in Section 3.1.1, the topo-clusters used to reconstruct jets have a direction relative to the center of the detector. However, as mentioned in Section 2.7, individual proton-proton interactions occur off-center along the beam axis rather than at the origin of the detector. Whilst keeping the jet energy constant, the origin correction recalculates the four-momentum such that the jet origin is at the primary vertex associated with the jet rather than the center of the detector. This correction improves the η resolution of the jets, but since the interaction location varies minimally in the x-y plane, this correction does little to the ϕ resolution [34, 33] [1].

3.2.2 Jet Area Based Pile-up Correction

As discussed in Section 2.7, each event is affected by pile-up. This jet area based correction corrects for the effects of pile-up by using two jet parameters. The area of a jet, A, which in an event is calculated using *FastJet* [35]. In the jet area calculation, infinitesimally low $\mathrm{p_T}$ "ghost particles" are distributed uniformly across the whole detector surface. The number of ghost particles associated with each jet gives a measure of the jet area. The pile-up energy density, ρ, defined as the median of the distribution of jet energy densities in the event. Where the energy density for each jet is given by p_T/A. The jet $\mathrm{p_T}$ after a correction based on these parameters is then $p_T^{corr} = p_T - \rho \cdot A$.

3.2.3 Residual Pile-up Correction

After the initial pile-up correction is applied, it is observed that the jet $\mathrm{p_T}$ is still affected by pile-up, requiring an additional residual correction. Because out-of-time pile-up is characterized by $< \mu >$ at fixed N_{PV}, and in-time pile-up is characterized by N_{PV} at fixed $< \mu >$, this residual correction is parametrized in terms of $< \mu >$ and N_{PV} as introduced in Section 2.8. The correction derived here is then applied as an additional step after the area-based pile-up correction.

3.2.4 Absolute JES and η Calibration

The absolute jet energy scale (absolute JES) calibration is a correction based on the relation between the reconstructed jet energy and the truth jet energy [36]. It is used to correct the reconstructed jet energy scale to the scale of truth jets, after pile-up subtraction. The correction factors used are defined as the inverse of the energy response, which is defined as $\mathcal{R}$ in Equation (3.1).

[1] It is worth noting that for newer ATLAS data, the origin correction is applied to the topo-clusters rather than the jets. The origin correction does therefore not need to be applied as part of the JES calibration chain as shown in Fig 3.4, which is from an earlier paper.

$$\mathcal{R} = \frac{E_{reco}}{E_{truth}} \tag{3.1}$$

Here, E_{reco} is the energy of a reconstructed jet, geometrically matched to a truth jet of energy E_{truth}, if they lie within $\Delta R = \sqrt{(\Delta\eta)^2 + (\Delta\phi)^2} = 0.3$. The average response for a given E_{truth} and $|\eta|_{det}$[2] is then defined as the mean of Gaussian fits to the response distribution in each E_{truth} and $|\eta|_{det}$ bin. The mean of these Gaussian fits as a function of $|\eta|_{det}$ then represents the jet response in a given sample as a function of $|\eta|_{det}$ [33]. The derivation of this response is similar to that used in this thesis, which is described in detail in Chapter 6.

After the absolute JES calibration has been applied, a bias in the reconstructed jet η is observed as a function of η_{det}. The bias is largest for jets which cover the transition region between two different calorimeter technologies. Different regions of the detector have different responses, therefore, a jet covering two different regions has an artificial increase to the energy on one side which alters the reconstructed four-momentum. To correct for this bias in η, further corrections are derived as the difference between the reconstructed and truth η, parametrized as a function of η_{det} and E_{truth}. This step affects the energy and momentum magnitude components of a jet, as well as its η [33]. Jets calibrated until this point are considered to be at the EM + JES scale.

3.2.5 Global Sequential Calibration (GSC)

Jet reconstruction and the response of jets are sensitive to fluctuations of the particle composition and energy distribution within a jet. These variables are in turn dependent on whether the particle initializing the jet is a quark or a gluon. A gluon jet often contains more particles with lower p_T which gives a wider transverse profile of the jet and a lower calorimeter response. A quark jet typically contains hadrons that carry larger fractions for the jet p_T and travel further in the calorimeter. After the previous calibration steps have been applied, it is observed that the response of a quark initiated jet compared to one from a gluon can vary by up to 8% [37]. In order to correct for this difference, five corrections are applied during the Global Sequential Calibration (GSC) step, based on tracking information, muon spectrometer information, and topology of energy deposits in the calorimeter. The GSC applies each correction independently and sequentially. Any correlation between the observables and the order of the corrections are ignored since taking these into account has not shown any improvements [33].

3.2.6 Residual In-situ Calibration

Most of the steps, except the pile-up correction, in the calibration so far have been based on Monte Carlo (MC) simulations of collision events, hadronization, particle interaction with the detector, etc. This means that if MC does not describe these processes correctly there will be residual effects not corrected for in data.

The in-situ calibration accounts for disagreement in the jet response between MC and data. These disagreements originate from MC's imperfect description of Quantum

[2]Here, $|\eta|_{det}$ is the jet $|\eta|$ in relation to the detector center, and the origin correction is reapplied afterwards.

Chromodynamics (QCD), electromagnetic, and hadronic interactions with the detector material. The idea of the in-situ calibration is to correct for the differences between MC and data by balancing the p_T of a jet against well-measured reference objects, and correcting the p_T in data using the ratio of these balances. This step contains three sub-steps: η-intercalibration, Z + jet and γ + jet balance, and multijet balance. For each sub-step we derive a correction factor, c, defined as the ratio between the MC p_T response, $\mathcal{R}^{MC}_{insitu}$, and the data p_T response, $\mathcal{R}^{data}_{insitu}$, as shown in Equation (3.2)

$$c = \frac{\mathcal{R}^{data}_{insitu}}{\mathcal{R}^{MC}_{insitu}} \tag{3.2}$$

As for the previous responses, the correction to the jet four-momentum is applied as a function of jet p_T. In the case of the η-inter-calibration, its correction is applied as a function of η [33].

η-intercalibration

The η-intercalibration uses dijet events to remove residual pseudorapidity differences. This is done by equalizing the p_T of jets in the non-central region to the p_T of balancing jets in the central region, because the central jets are considered well measured [33].

$Z + jet$ and $\gamma + jet$ Balance

In contrast to the η-intercalibration, the $Z + jet$ and $\gamma + jet$ calibration uses p_T balance of jets against a Z boson or photon to calibrate jets in the central region up to 950 GeV. This sub-step, therefore, relies on the independent energy calibration and measurement of the Z bosons leptonic decay products and/or the photon. Regardless of this dependence, these are good candidates because the electrons, muons, and photons can be measured very precisely in ATLAS. At high p_T , the γ+jet calibration is statistically limited by the small number of events for this process. This gives the γ+jet calibration a limit of 36 $<p_T<$ 950 GeV. Because of the same reasons, the p_T range of the Z+jet calibration is limited to 20 $<p_T<$ 500 GeV [33].

Multijet Balance

The multijet balance is used to extend the p_T range of the in-situ calibration up to ≈ 2 TeV. Under the assumption that the p_T of two recoiling objects is the same, events with three or more jets are used to balance the p_T of a high-p_T jet to to the p_T of a recoiling system of several low-p_T jets. A p_T limit of 950 GeV is imposed on the low-p_T jets such that they are fully calibrated through the Z/γ+jet calibration. This limit means that events with very high-p_T leading jets, which have recoiling jets of p_T >950 GeV are rejected. Such high-p_T events are however recovered by using multiple iterations of the multijet balance, where previously derived calibrations are applied on the high p_T recoiling jets [33]. In the most recent derivation, the multijet balance reached a maximum p_T bin of central value 2291 GeV with an upper edge at 2415 GeV [38]. This means that above 2415 GeV, the calibration cannot be corrected using in-situ. Instead, an uncertainty is applied due to the lack of knowledge above this p_T , based on a component-wise derivation, using

the single particle response in MC and data, to extrapolate a correction factor for jets. This component-wise derivation is discussed further in Section 5.1.

In-situ Combination

Resulting from each of the above three in-situ calibration sub-steps is a data-to-MC ratio, seen in Equation (3.2), as a function of jet p_T or η. As discussed above, these corrections are valid within different p_T ranges and have to be combined. The combination is done as follows: For each sub-step, the results are put in the same fine p_T binning by interpolating it with a second-order polynomial spline. Each bin in each of the three splines is assigned a p_T-dependent weight depending on the data-to-MC ratio and their uncertainties in each p_T bin. These weights are then used to calculate a weighted average of the three splines for each p_T bin. Finally, a sliding Gaussian kernel is used to smooth this average.

For analysis methods with extremely large statistics such as Trigger-object Level Analysis (TLA), discussed in Section 5.2, using this spline-based smoothing procedure for the in-situ calibration can be problematic. In these searches, the statistical uncertainty from the relatively small in-situ Z/γ+jet data sets is larger than the statistical uncertainty in each of the bins. This has historically lead to problems where fluctuations in the final in-situ spline have induced signal-like bumps in the final TLA analysis. How the work of this thesis can be used to address this issue in the future is discussed in Section 5.2.

3.2.7 Jet Energy Scale Calibration Uncertainty

The overall uncertainty of the JES calibration is made from a set of 80 systematic uncertainty terms originating from the individual calibration steps. A list of uncertainties can be found in [33]. For high-p_T jets beyond the 2415 GeV limit of the in-situ calibration, an uncertainty is derived from single-particle response studies, where uncertainties on single particles constituting a jet are propagated to the jet itself and combined [39].

Uncertainties can be derived in different η and p_T regions. As seen in Figure 3.5 the whole uncertainty abruptly increases after 2415 GeV where the range of in-situ ends and the uncertainties come from the propagation of single-particle responses [33]. Updating these single particle uncertainties is a core part of this thesis and will be discussed further in Section 5.1.

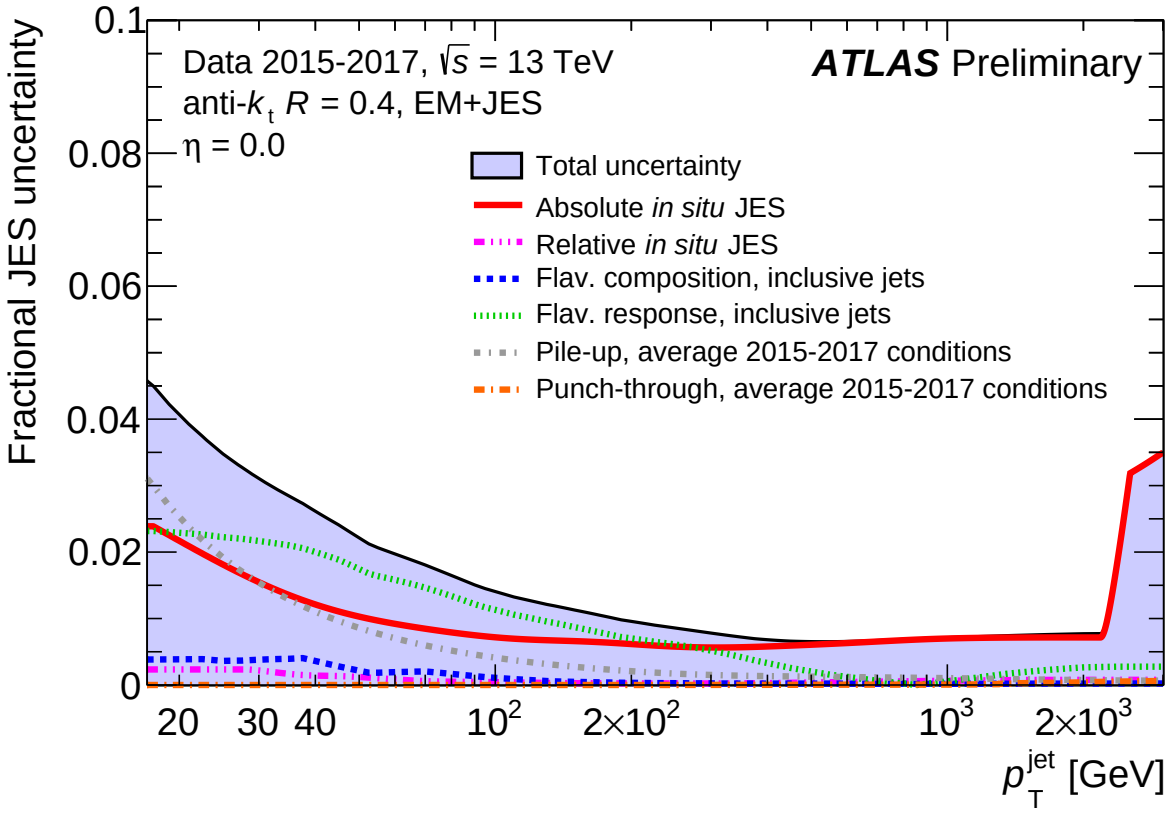

Figure 3.5: The combined total and individual components of the Jet energy Scale (JES) calibration uncertainty of fully calibrated jets, as a function of p_T in the central region [40].

Chapter 4

Particle Interaction with Matter

In order to detect a particle, the particle has to interact with the material of the detector. The following sections will discuss the different particle interactions with matter necessary to understand the properties of the ATLAS detector, as well as details of how these interactions are simulated and the different variations to such simulations relevant to this thesis.

4.1 Electromagnetic Interactions

Charged particles can interact electromagnetically with the detector material. The two main interaction processes for electromagnetic energy loss are ionization and radiative energy losses.

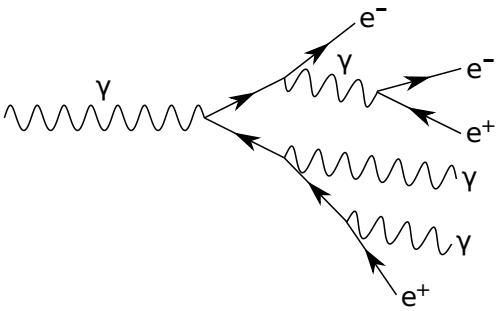

Figure 4.1: A visual representation of how bremsstrahlung and pair production creates the cascading chain reaction giving rise to what is called a particle shower

During ionization, a charged particle excites atomic electrons, a process through which the particle loses an amount of energy per unit length as given by the Bethe-Bloch formula [5]. The important feature of the Bethe-Bloch formula is that the rate of energy loss is the largest for low-velocity particles, and that it is dependent on the particle mass. For electrons at low energy, ionization is the main process for energy loss. We define a critical energy for electrons $E_c \approx 800/Z$ MeV, where Z is the atomic number of the medium. Above this energy, radiative processes dominate the energy loss.

For radiative energy loss, a charged particle traversing the strong electrostatic fields of nuclei radiates photons, a process called bremsstrahlung. All charged particles can undergo bremsstrahlung, however, the rate of energy loss through bremsstrahlung is inversely proportional to the square of the particle mass. This means that both ionization and bremsstrahlung are relevant for different particles at different energies [5].

Due to the emission of photons from bremsstrahlung, an important aspect in detecting energy deposition is the interaction of photons with matter. For this thesis, we are

concerned with how photons interact with matter through three main processes [5]:

- Low energy photons interact mainly through the photoelectric effect, where a photon is absorbed by an atomic electron which is then ejected from its bound state of the atom.
- Above 1 MeV, Compton scattering becomes significant, where the photon scatters off an atomic electron.
- For energies above 10 MeV, the energy loss is dominated by Electron-positron pair production. This is a process where the energy of a photon is converted to an electron and a positron pair, according to $E = mc^2$. This is only possible if the initial photon energy is larger than twice the electron mass and it can only occur in the presence of the electrostatic field of a nucleus in order to conserve the momentum of the photon through the recoiling nuclei.

At high enough energy, the electron and positron created from pair production can on their own produce bremsstrahlung with enough energy to create more electron-positron pairs in a cascading chain reaction [3]. Such a cascade is called a shower and is for the electromagnetic interaction visualized in Figure 4.1. A quantity used to characterize these showers is called the radiation length, where one radiation length is the average distance over which the energy of a high-energy electron is reduced by a factor $1/e$ through bremsstrahlung. This distance is approximately the same as $\frac{7}{9}$th of the average distance traveled by a high-energy photon in between electron-positron pair productions [41, 5].

Electromagnetic showers as in Figure 4.1 stop developing when the average energy of the particles is less than the critical energy. This means that, due to their relatively short radiation length, a 100 GeV shower in lead stops developing after roughly 10cm [5]. Because of this small traversed distance, the energy of an electromagnetic shower is deposited in a small region of space. Furthermore, the large number of same-species particles in an electromagnetic shower means that electromagnetic showers of the same energy fluctuate very little in their properties [5].

4.2 Hadronic Interactions

At short ranges, hadrons can interact strongly with atomic nuclei, regardless of their electric charge. There are multiple hadronic interactions with matter, however, we will first discuss the elastic and inelastic interactions. The others are discussed in some more detail in Section 4.3. In the simple case of a one proton nucleus as a target, an elastic scattering could be the following

$$\pi^- + p \rightarrow \pi^- + p \tag{4.1}$$

where the initial and final particles are the same. For an inelastic case such as

$$\pi^- + p \rightarrow \pi^+ + \pi^- + \pi^0 + n \tag{4.2}$$

the initial and final particles are not the same [3]. At high enough energies the particles produced from an initial strong inelastic scattering can interact further with the target

material, either electromagnetically or hadronically, to create a cascade of particles called a hadronic shower. Similarly to electromagnetic showers, we define a nuclear interaction length. This is defined as the average distance between hadronic interactions of relativistic hadrons [5]. This nuclear interaction length is much larger than the radiation length for electrons and photons, which means that compared to an electromagnetic shower, a hadronic shower covers a much larger volume in space. Furthermore, because of the large variety of final states available in hadronic interactions, the differences between hadronic showers of the same energy is much larger than for electromagnetic showers of the same energy. As an example, due to the $\pi^0 \to \gamma\gamma$ decay, a hadronic shower with a π^0 in the early stages may develop to be a predominantly electromagnetic shower. In this way, properties of hadronic showers fluctuate more than for electromagnetic showers [5]. Another problem with hadronic showers is the use of non-compensating calorimeters, as introduced in Section 2.8. Non-compensating calorimeters do not compensate for the energy lost in the form of nuclear break-up and excitation. From this lack of compensation, on average 30% of the jet energy incident on the non-compensating hadronic calorimeter is lost [5].

Because of the fluctuations and complex development of hadronic showers, it is difficult to guarantee that they are modeled correctly when simulating particle interaction in ATLAS. There are many different models for different hadronic and nuclear processes, the use and combinations of such models will be discussed in Section 4.3

4.3 Hadronic Shower Models

Simulating particle interactions with the detector is done with the ATLAS software framework ATHENA [42] using the Geant4 [32] simulation tool-kit. As simulated particles traverse through the detector electromagnetic, hadronic, and photo-nuclear interactions are simulated. Geant4 uses collections of multiple models to simulate particle interactions with matter, where the particle type, its energy, and the material it's propagating through, all determine what collection of models is suitable. Following are brief descriptions of some of these individual models [43].

- At the high energies of the initial hadron-nucleon collision, the High Energy Parametrized model (`HEP`) can be used for long-lived particles (lifetime longer than 10 ps). This is a parameterized model, meaning that it is based on measured and extrapolated reaction cross-sections for particle distributions in order to simulate the hadronic showers. Parametrized models are fast, but lack some details and cannot guarantee energy and momentum conservation for each interaction [44].

- Complementary to `HEP` at the high energies are the Fritiof string model (`FTF`) and the Quark-gluon String model (`QGS`). These are theory based interaction models, meaning that they rely more on simulation of the fundamental processes in the interactions than the extrapolation of measurements [44].

- At lower energies, cascade models are used. Two of these are the theory based Binary Nucleon-nucleon Scattering model (`BIC`) and the less theory based Bertini Nucleon-nucleon Scattering (`BERT`) model.

- At the low energies, there is also the Low Energy Parametrized model (`LEP`), which is sometimes used to covers the transition between the low energy cascade models and the high energy string models.

- The precompound model (`P`) is used to model the de-excitation of nuclear remnants after high energy interactions. This can be added to both `FTF` and `QGS` to create the `FTFP` and `QGSP` models respectively. However, when `BERT` is used, its own simpler precompound and de-excitation models are used for the same purposes.

- Very low energy particles can be re-absorbed by a nucleus, according to the Chiral Invariant Phase Space model (`CHIPS`).

- The High-precision neutron model (`HP`) provides precise models for neutron-nucleus interactions and neutron transport, for neutrons from thermal energies up to 20 MeV.

- A specific transition energy range between `BERT` and `FTF` as required by the ATLAS experiment (`ATL`) where BERT and FTF overlap in the 9-12 GeV energy range [45].

- Unless stated otherwise, a standardized model is used to model electromagnetic interactions. In this thesis, a variation of the standard called electromagnetic option 3 (`EMY`) is used. `EMY` adds high-precision EM processes but is slower to simulate than the standard [45].

Collections of these models are called physics lists. A physics list is a consistent collection of models such that it covers the interaction of all particles in the whole applicable energy range [44]. A physics list includes many different models of different interactions for different particles, but since this thesis is looking at differences between physics lists, we will only focus on the individual models which differ between our physics lists. A visualization of how the models in a physics list consistently cover the energy range for different particles is shown in Figure 7.1. As can be seen in this figure, as the energy increases where two models overlap in particle type and energy, the probability of the low energy model being used decreases linearly from 1.0 to 0.0, and the higher energy model is used with an increasing complementary probability from 0.0 to 1.0 [46]. This simple linear transition means that the color combination at a given energy in Figure 7.1 is directly proportional to the probability for the model associated with the color to be used for a particle at that energy.

The physics lists used in this thesis are found in Table 4.1. `FTFP_BERT_ATL` is the physics list used for creating the Monte Carlo (MC) samples used in calibration and other procedures at ATLAS, and it is therefore called the *nominal*. For each physics list, Table 4.1 also contains short descriptions of the physics list specific models which differ from the nominal, for a full description see [47]. Because of the large model deviations of the `QGSP` based physics lists, the best overview for these with respect to the nominal is seen in Figure 7.1.

This thesis also compares different geometry lists. In a geometry list, the modeling of physical processes uses the nominal physics list, but details of the detector material composition or layout have been changed for the different geometry lists.

Tag	Physics List Name and Description
s3170	`FTFP_BERT_ATL` (Nominal) • `BERT` for all particles ($p, n, \pi^+, \pi^-, K^+, K^-, K_L, K_S, \Lambda, \Sigma^+, \Sigma^-, \Sigma^0, \Xi^-, \Xi^0$ and Ω^-) between 0-12 GeV. • `FTFP` for all particles between 9 GeV-100 TeV.
s3331	`FTFP_BERT_ATL_EMY`: High-precision EM processes
s3332	`QGSP_BIC_HP_EMY`: A different set of elastic cross sections is used for kaons, more accurate transportation of neutrons below 20 MeV, high-precision EM processes • `BERT` is used for only π^+, π^-, K^+, K^-, K^0_L, K^0_S, $\Lambda, \Sigma^+, \Sigma^-, \Sigma^0, \Xi^-, \Xi^0$ and Ω^- between 0-5 GeV. This subset of particles is indicated by (*) in Figure 7.1 • `BIC` is used for n and p between 0-9.9 GeV. This subset of particles is indicated by (**) in Figure 7.1 • `FTFP` is used for hyperons ($\Lambda, \Sigma^+, \Sigma^-, \Sigma^0, \Xi^-, \Xi^0$, and Ω^-) between 4 GeV-100 TeV. This subset of particles is indicated by (***) in Figure 7.1 • `QGSP` is used for all particles except hyperons above 12 GeV • `FTFP` is used for all particles except hyperons between 4 GeV-25 GeV
s3333	`FTFP_BERT_ATL_noDiffraction`: Both projectile and target direction are switched off
s3334	`QGSP_FTFP_BERT_ATL`: • `BERT` for all particles between 0-12 GeV • `FTFP` for all particles between 9-25 GeV • `QGSP` for all particles between 12 GeV-100 TeV
s3335	`FTFP_BERT_ATL_rescattering`: Re-scattering of the final-state produced by FTF is simulated with BIC
s3336	`FTFP_BERT_ATL_chipsXS`: Different inelastic hadron-nucleus cross-sections
s3337	`FTFP_BERT_ATL_HP`: Transportation of neutrons below 20 MeV is more accurate

Table 4.1: List of all physics lists used in this thesis including a tag for reference and a description of the specific models which differ with respect to the nominal physics list. The details of each physics list was either obtained through their MC generation request or from the Geant4 documentation found at [47].

Tag	Geometry List Name and Description
s3170	`FTFP_BERT_ATL` (Nominal)
s3360	`ATLAS-R2-2016-01-00-02` : 5% more material in Inner Detector
s3369	`ATLAS-R2-2016-01-00-14` : Additional material between EM calorimeter and hadronic calorimeter
s3370	`ATLAS-R2-2016-01-00-15` : Pre-EM calorimeter distorted geometry with changes to all of inner detector endplate, barrel cryostat, transition region, after barrel presampler, and after endcap presampler
s3371	`ATLAS-R2-2016-01-00-16` : Additional material in specific regions of the inner detector

Table 4.2: List of all geometry lists used in this thesis including a tag for reference and a description of the specific geometric variations with respect to the nominal physics list. The details of each geometry list was obtained through their generation request

Chapter 5

Introduction to Thesis Work and its Relevance

This chapter will introduce the details of the motivations for this thesis. First is a brief introduction to how single hadron response uncertainties are extrapolated to the Jet Energy Scale (JES) uncertainty, why the K_L^0 response is a dominant contribution to this uncertainty, and how this thesis aims to derive an improved K_L^0 response uncertainty. Second is an introduction to Trigger-object Level Analysis (TLA), how it achieves a larger number of recorded events than traditional analyses, how the in-situ step of the JES calibration is problematic for TLA, and how the tools developed in this thesis will be used in the future to address these issues.

5.1 Single Particle Response Uncertainty Extrapolation to Jet Energy Response Uncertainty

The JES calibration, as discussed in Section 3.2, is an important input to many jet-based analyses at ATLAS. As shown in Figure 3.5, the main contribution to the uncertainty of this calibration is from the data-driven in-situ calibration. However, as discussed in Section 3.2.6, the in-situ method is only valid up to 2415 GeV. Beyond 2415 GeV a component-wise derivation of the jet response uncertainty is used to determine the uncertainty, also called *single particle uncertainty*.

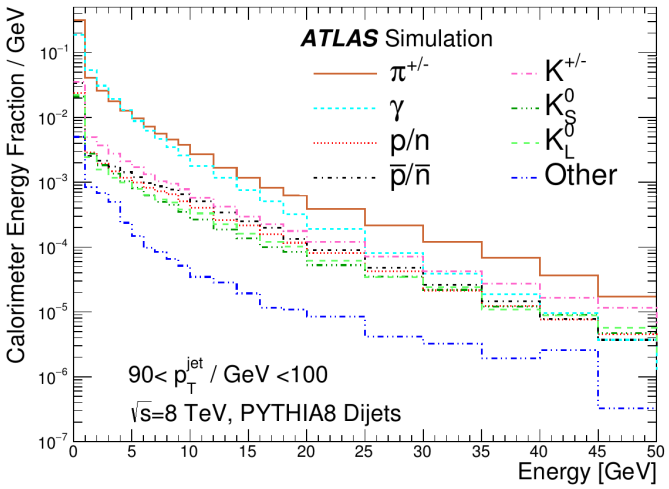

Figure 5.1: The spectra of fractional jet energy deposited per particle species in the calorimeter as a function of jet energy [39].

In this component-wise derivation, distributions of the jet energy fraction deposited in the

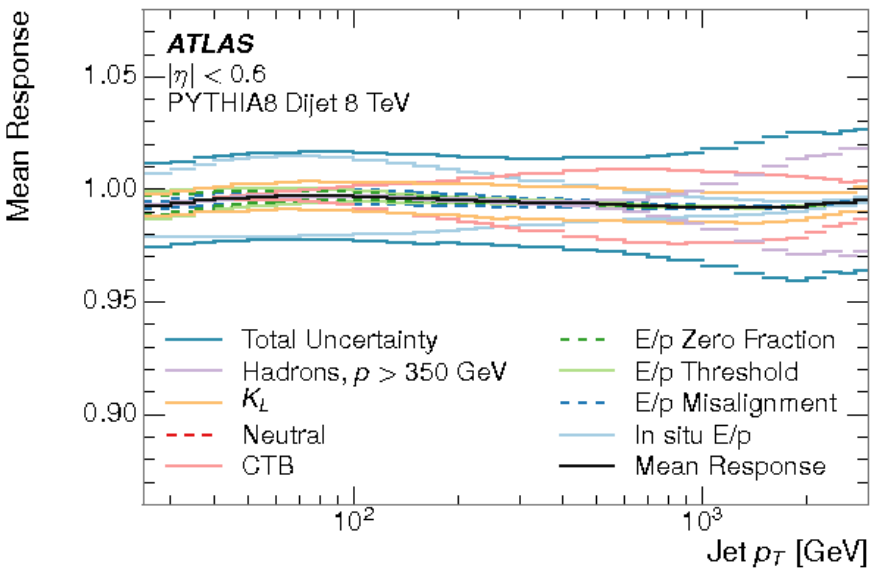

Figure 5.2: The mean response derived as the double ratio of simulated particle responses compared to single particle response in data, propagated to jets. For our purposes, this serves as a indicator of the individual contributions to the total Jet Energy Scale (JES) calibration uncertainty [39].

calorimeter for each particle, as
shown in Figure 5.1, is obtained from Monte Carlo (MC) simulation. Each of the particles in the MC simulation can then be assigned an uncertainty based on its type, and propagated to jets in order to derive a JES uncertainty [39]. The uncertainties for some of the charged particles can be measured by comparing the energy deposited in the calorimeter to the momentum measured by their associated track. However, neutral particles such as the K_L^0 leave no tracks and its associated uncertainty is therefore currently estimated conservatively to be 20% over the entire p_T range.

As seen in Figure 5.2 this K_L^0 response uncertainty propagated to jets is one of the main contributions to the JES uncertainty above 2415 GeV [39]. Therefore, the main aim of this thesis is to use the tools developed in order to derive a lower K_L^0 response uncertainty than what is currently used. The uncertainty will be determined by evaluating how the K_L^0 response changes between different physics lists compared to the nominal and taking the envelope of these differences. If a lower K_L^0 uncertainty is derived, it will improve the total uncertainty of the JES calibration used for multiple jet searches and analyses at ATLAS. Since there are no K_L^0 geometry list MC samples, the response for different physics lists and geometry lists of π^+ and π^- will also be investigated. If the general behavior for the pions and the K_L^0 are similar for the physics list variations, then the result for the pion geometry lists will be used to decide what geometry lists should be generated for K_L^0. This is done so that these samples can be used in future K_L^0 response studies.

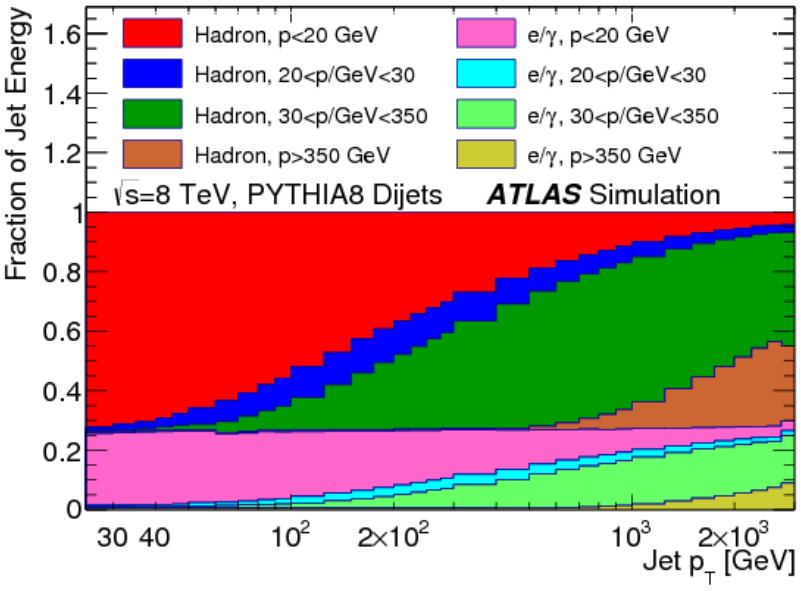

Figure 5.3: The fraction of jet energy carried by different particle species, at different energies, as a function of jet energy [39].

5.2 Trigger-object Level Analysis (TLA)

TLA is a type of data recording technique that has been introduced at ATLAS by a group of ATLAS researchers including those from the Lund group. The idea is to increase the number of recorded events by using a smaller event size. To accomplish this, TLA only records the jets that have been reconstructed by the High-level Trigger (HLT) from the calorimeter information. This means that TLA can record a lot more events than a regular jet analysis. Figure 5.4 shows the increased amount of events recorded by TLA in the sub-TeV invariant mass region, compared to the conventional jet analysis. The decreased statistical uncertainty increases our sensitivity to find new resonant particles in the lower parts of the invariant mass spectra.

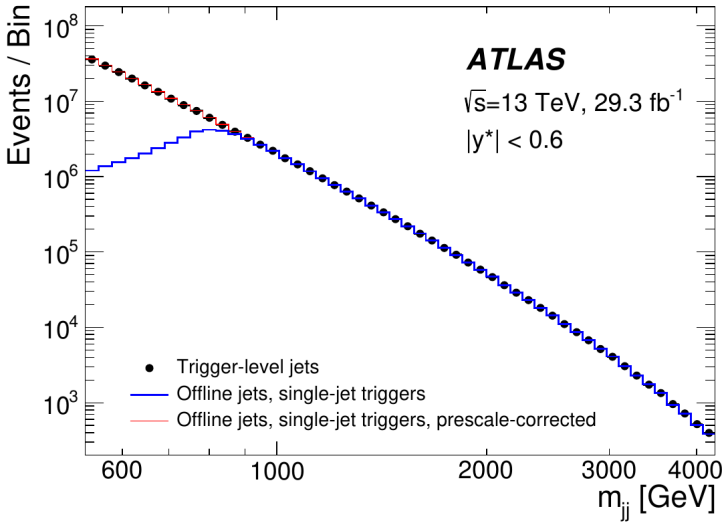

Figure 5.4: The number of full dijet events from single-jet triggers (blue) which are prescaled (only a fraction of events are recorded), compared to the number of trigger level dijet events in the data used by TLA (black points) [48].

There are however multiple issues for TLA working with a subset of the event information. Since the events do not have any tracking or muon information, the GSC in the JES calibration, discussed in Section 3.2, has to be tailored specifically for TLA. A new calibration step also has to be added to the JES calibration, which corrects for residual differences between trigger-level jets and offline jets [48]. Furthermore, because of the low statistical uncertainties associated with TLA, statistical uncertainties in the JES calibration can become dominant. This is problematic for the in-situ calibration because statistical fluctuations from the relatively small in-situ data set have a risk of inducing signal like features in the TLA analysis. The ratio plot at 300 GeV in Figure 5.5 shows such a bump in the in-situ response, which can generate such a signal-like feature.

Therefore, one of the aims of this thesis is to develop software tools which can derive and present jet energy and transverse momentum responses from different data sets. The end goal for these tools is to be used for investigating the different responses after each of the TLA JES calibration steps. It is essential that after each calibration step, the jet response is smooth so that none of the calibration steps can introduce signal-like features in the analysis. This code developed for this purpose is described in Section 6.

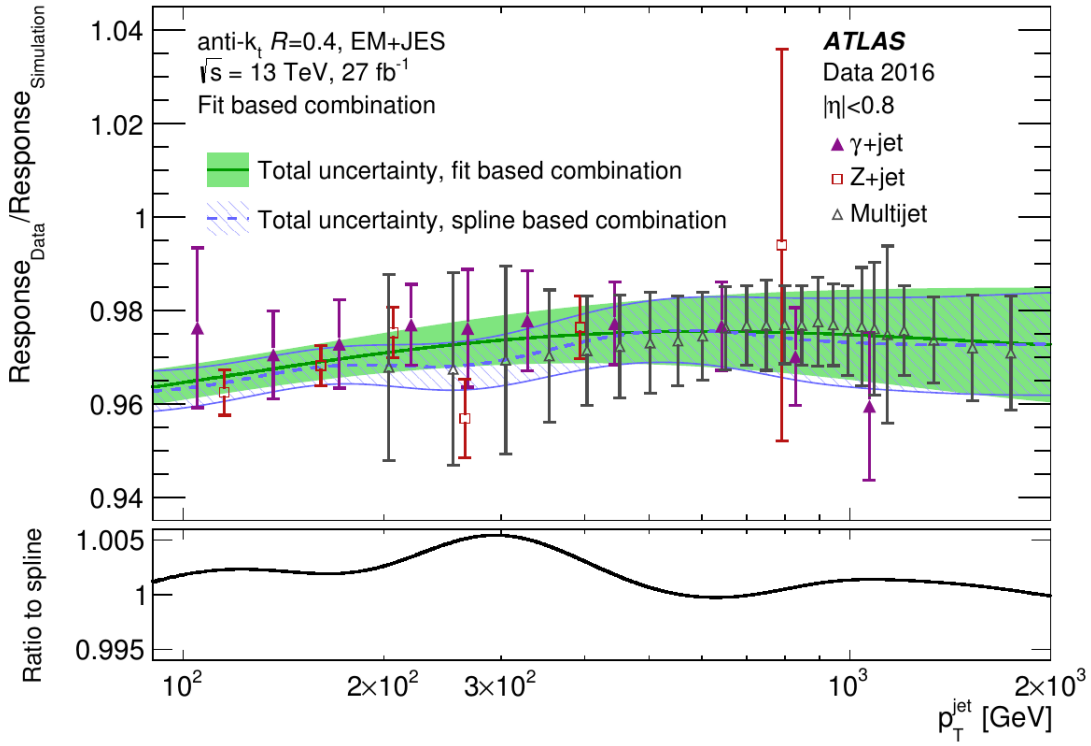

Figure 5.5: A comparison between using a fit- or spline-based method for the in-situ combination. The ratio between the two methods is shown in the bottom panel. As seen at 300 GeV, this ratio suggests that spline-based methods risk introducing signal-like features in the analysis [48].

Chapter 6

Methods and analysis

This chapter describes the software tools developed in this thesis how they work and how they are used to produce response plots and comparisons between responses from different physics and geometry lists. This chapter focuses on the different methods and code used so that this chapter can serve as an introduction to the features of the code for future potential users.

As discussed in Section 5.1 this thesis will derive a new K_L^0 response uncertainty by studying how its response varies between different physics lists. This is in practice done by producing response plots for different physics lists and looking at their ratio to the nominal physics list. For this thesis the physics and geometry lists in Table 4.1 and 4.2 were used. The processing of these to produce the final response and response ratio plots is shown as a flowchart in Figure 6.1, and described below.

1. Before this work, so called *Particle Gun* MC samples had been generated. In the generation of such samples, each event is generated by simulating the desired particle species being sent, one per event, from the center of the detector with a random four-momentum and probability to decay. The resulting particle interactions with the detector material are then simulated with Geant4 using the specified physics list.

2. A NTuple is a file of a data format which is readable by the ROOT 6 [49] framework used for analysis in this thesis. These NTuples were generated for each MC sample and contain event by event information of reconstructed clusters, reconstructed jets, truth particles and more.

3. The NTuples, one for each physics list, are used as inputs for `makeResponsePlots.cxx` [50]. This algorithm iterates over all the events in the NTuple, and for each event iterates over all the truth particles. For each truth particle it geometrically matches all reconstructed clusters within $R = \sqrt{\phi^2 + \eta^2} = 0.2$ to that truth particle. The four-vectors of the clusters matched are then summed into one four-vector. Finally, the p_T response is then calculated from the p_T of the combined cluster four-vector and the p_T of the truth particle. A 3D histogram binned in p_T response, truth p_T , and truth $|\eta|$ is then filled with the response value corresponding to this match.

4. The generated 3D histogram is used as input for a Python 2 [51] function called `TH3toTGraph` [50]. This script iterates over user defined slices, for example $0 < |\eta| < 0.6$ and $0.6 < |\eta| < 1.1$. It isolates the slices of the 3D histogram, and projects the data in that slice into a 2D histogram. As an example, if we took a slice in $|\eta|$, that 2D histogram would have the response on its y-axis and the truth p_T on its x-axis. The script then iterates over each p_T bin on the x-axis of the 2D histogram and projects that content into a 1D histogram. This results in a 1D histogram for each truth p_T bin, containing the distribution of p_T responses for all events in that particular p_T bin and $|\eta|$ slice. This distribution is then fitted with a Gaussian, the fit is optimized using the `JES_BalanceFitter.py` [52].

5. After the iteration over $|\eta|$ slices and p_T bins, for each physics list we obtain one graph of p_T response vs $p_{T\ truth}$ per $|\eta|$ slice. Where the p_T response is the mean of the Gaussian fit for each bin.

6. `PhysicsListComparison.py` [50] is a Python 2 script which for each of the $|\eta|$ slices defined earlier, collects all the p_T response graphs of each physics list and plots them on the same canvas. This results in one plot showing the p_T response of all physics lists, and their ratio to the nominal physics list, for each $|\eta|$ slice. These plots are presented as results and discussed in Section 7

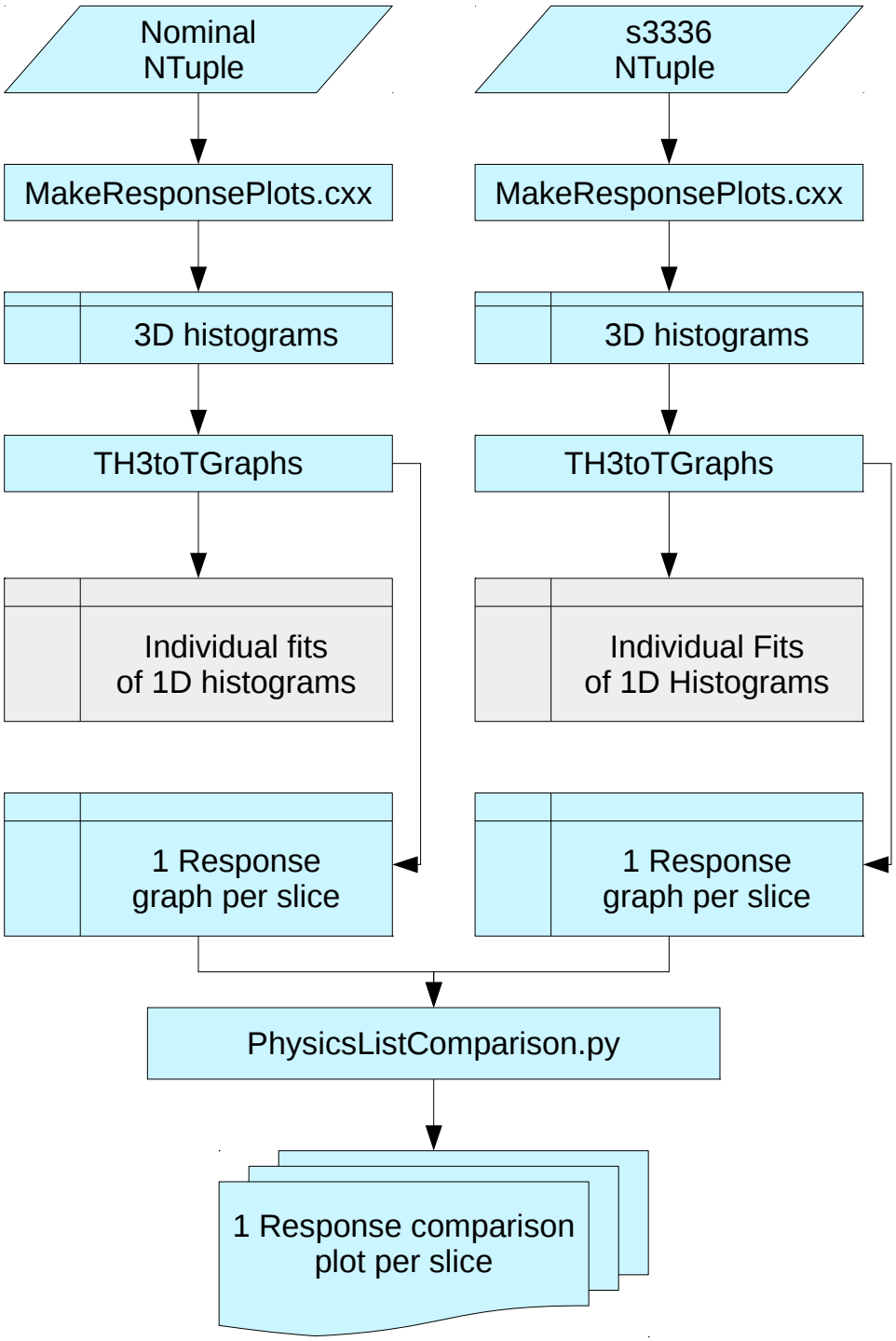

Figure 6.1: Flowchart showing the process including the scripts and functions developed in this thesis which produces response comparison plots. In this example an NTuple of the nominal and the `FTFP_BERT_ATL_chipsXS` (s3336) physics list is used. This process is expandable to any number of physics lists.

Chapter 7

Results and Discussion

This chapter presents the results, with associated discussion, from this thesis work. Presented first is the response and response ratio as a function of truth p_T for the K^0_L and the pions. For these plots, the behaviors of the physics lists deviating the most from the nominal are presented together with the most probable causes for the deviations. Second is a presentation of the pion geometry list variations, which are used to conclude which geometry list Monte Carlo (MC) samples should be generated for the K^0_L. Presented last is the derivation of the improved K^0_L response uncertainty using the K^0_L response and response ratio as a function of truth p_T for the different physics lists.

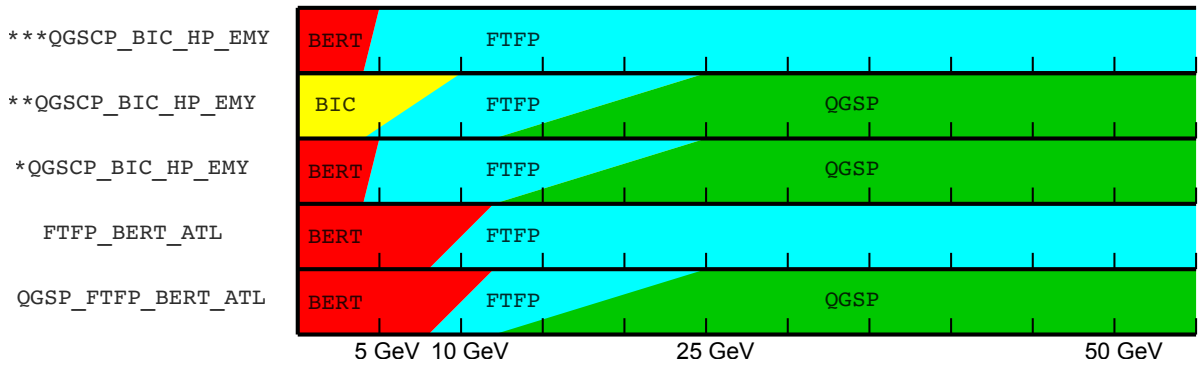

Figure 7.1: A visualization of three different hadronic physics lists used for different particles in different energy regions, *FTFP_BERT_ATL* being the nominal. The amount of color at a given energy is directly proportional to the probability for a model associated with the color to be used for a particle at that energy. Details of each physics list in this figure can be found in Table 4.1.

7.1 Physics List Variations

7.1.1 QGSP_FTFP_BERT_ATL(s3334)

For QGSP_FTFP_BERT_ATL in Figure 7.1 we see that compared to the nominal (FTFP_BERT_ATL), it has FTFP and QGSP overlapping from 12 GeV-25 GeV and only QGSP above 25 GeV. Figure 7.2a and 7.2b show the K_L^0 p_T response as a function of truth p_T, the slices for $0.0 < |\eta| < 0.6$ and $0.6 < |\eta| < 1.1$ respectively. Figure 7.3 and 7.4 show the same plots for π^+ and π^- respectively. In the response ratio of all these figures, QGSP_FTFP_BERT_ATL has a deviation with an increasing slope in the 10-25 GeV region, followed by a decreasing slope in the 25-200 GeV energy region. Since the only difference between QGSP_FTFP_BERT_ATL and the nominal is the use of QGSP above 12 GeV, we can correlate the overlapping FTFP and QGSP to the increasing slope in the 10-25 energy GeV region, and correlate the decreasing slope in the 25-200 GeV region to the sole use of QGSP above 25 GeV.

As can be seen in Figure 7.2, 7.3, and 7.4, there are large fluctuations outside the uncertainties of the response ratio data points below 3 GeV. These fluctuations are due to fit instability of low p_T histograms with a low number of entries. These fits are discussed further in Appendix A.1. Regardless of the bad fits, as seen in Figure 5.3, above 2000 Gev the main hadronic contribution to the total jet energy comes from hadrons of $p_T >$ 350 GeV. Therefore, these fluctuations are not a major concern, since the K_L^0 response uncertainty extrapolated to the Jet Energy Scale (JES) uncertainty is not currently in use below the 2415 GeV limit of the in-situ calibration.

7.1.2 QGSP_BIC_HP_EMY (s3332)

Without accounting for its sub GeV neutron simulations and high precision electromagnetic models, QGSP_BIC_HP_EMY for protons and neutrons in Figure 7.1 uses BIC in the 0-10 GeV energy region overlapping with FTFP from 4-10 GeV. Followed by FTFP for 10-12 GeV, overlapping with QGSP between 12-25 GeV and finalized by only QGSP above 25 GeV. For all particles except protons and neutrons, it uses BERT in the 0-5 GeV region, overlapping with FTFP from 4-5 GeV. Followed by FTFP for 10-12 GeV, overlapping with QGSP between 12-25 GeV and finalized by only QGSP above 25 GeV. By looking at the distribution of particles in our nominal K_L^0 MC samples, it was found that they contain less than 0.5% hyperons ($\Lambda, \Sigma^+, \Sigma^-, \Sigma^0, \Xi^-, \Xi^0$, and Ω^-). Therefore we will not include the hyperons in our following discussions.

The response ratios in Figure 7.2, 7.3, and 7.4 show that QGSP_BIC_HP_EMY has a bump-like deviation in the 3-10 GeV region. Because of the use of multiple models for different particles in this region, it is difficult to correlate a specific model combination to such a deviation. However, the deviation is likely a result of the lower range energy BERT and FTFP together with BIC for protons and neutrons, compared to the nominal use of only BERT.

Furthermore, from Figure 7.1 we see that QGSP_BIC_HP_EMY and QGSP_FTFP_BERT_ATL use the same hadronic models in the same proportions above 12 GeV. Looking again at QGSP_BIC_HP_EMY in Figure 7.2, 7.3, and 7.4 we see a second deviation in the 10-25 GeV region. Assuming that HP and EMY have little influence, the majority of the second deviation is then correlated to the overlapping FTFP and QGSP in the 10-25 GeV

region and the sole use of QGSP above 25 GeV, just like for QGSP_FTFP_BERT_ATL. The observed small deviations between QGSP_BIC_HP_EMY and QGSP_FTFP_BERT_ATL could be attributed to either HP and EMY, but possibly also from QGSP_BIC_HP_EMY using different elastic scattering cross sections for kaons.

7.1.3 FTFP_BERT_ATL_noDiffraction (s3333)

From Table 4.1 we know that the only difference between FTFP_BERT_ATL_noDiffraction and the nominal is that this physics list does not model projectile and target directions. Figure 7.3 and 7.4 show a deviation of FTFP_BERT_ATL_noDiffraction around 10 GeV, but the magnitude and spread of the deviation varies between the particle species and η slice. However, since noDiffraction is the only difference between this physics list and the nominal, we can correlate the use of noDiffraction to the observed deviation. It is important to note that this deviation is not observed for the K_L^0 in Figure 7.2. It is possible that this deviation only occurs for charged particles, but further investigations would have to be made to conclude that. Since this deviation is so small in relation to the other physics list variations, it will not affect our K_L^0 uncertainty derivation.

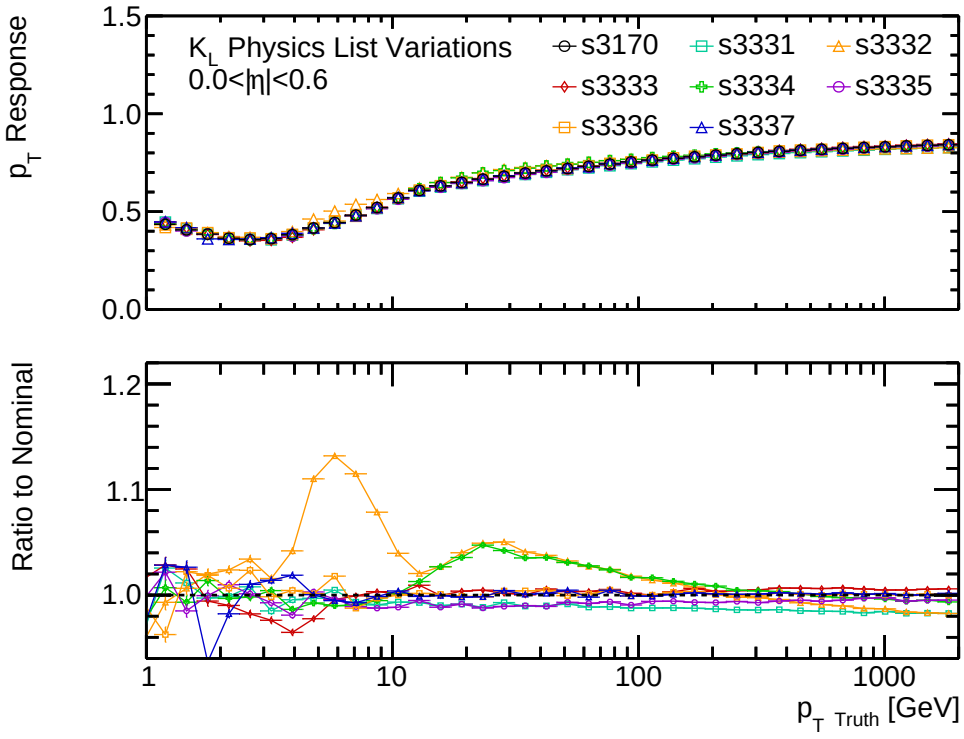

(a)

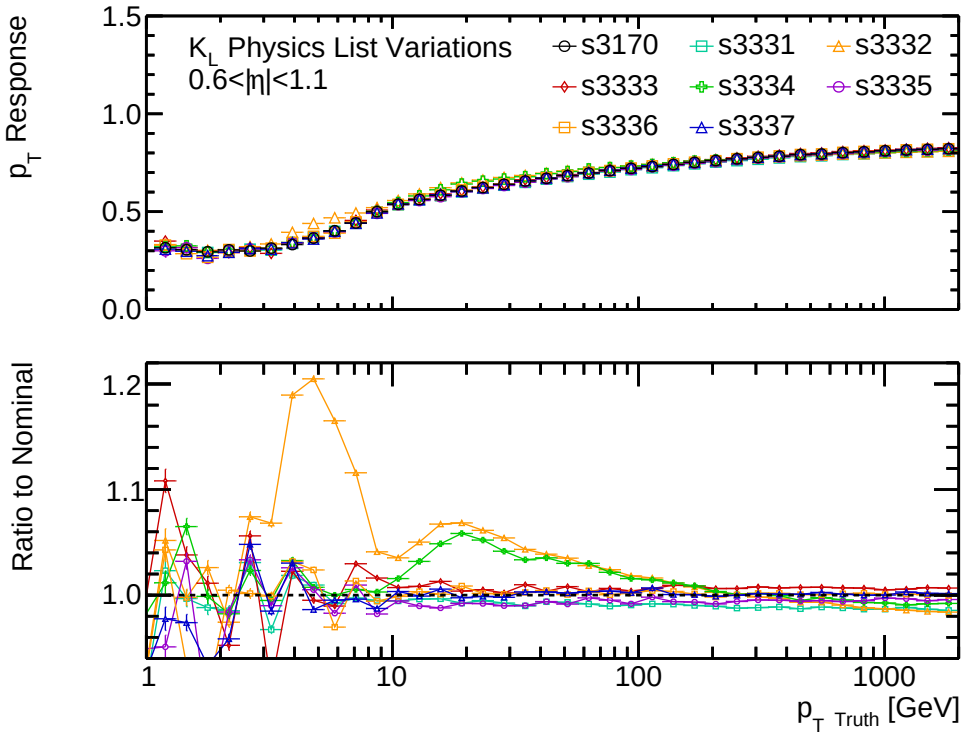

(b)

Figure 7.2: K^0_L p_T response and response ratio of different physics lists compared to the nominal as a function of truth p_T, sliced in $0.0 < |\eta| < 0.6$ (a) and $0.6 < |\eta| < 1.1$ (b). The physics list corresponding to each tag in the legend can be found in Table 4.1.

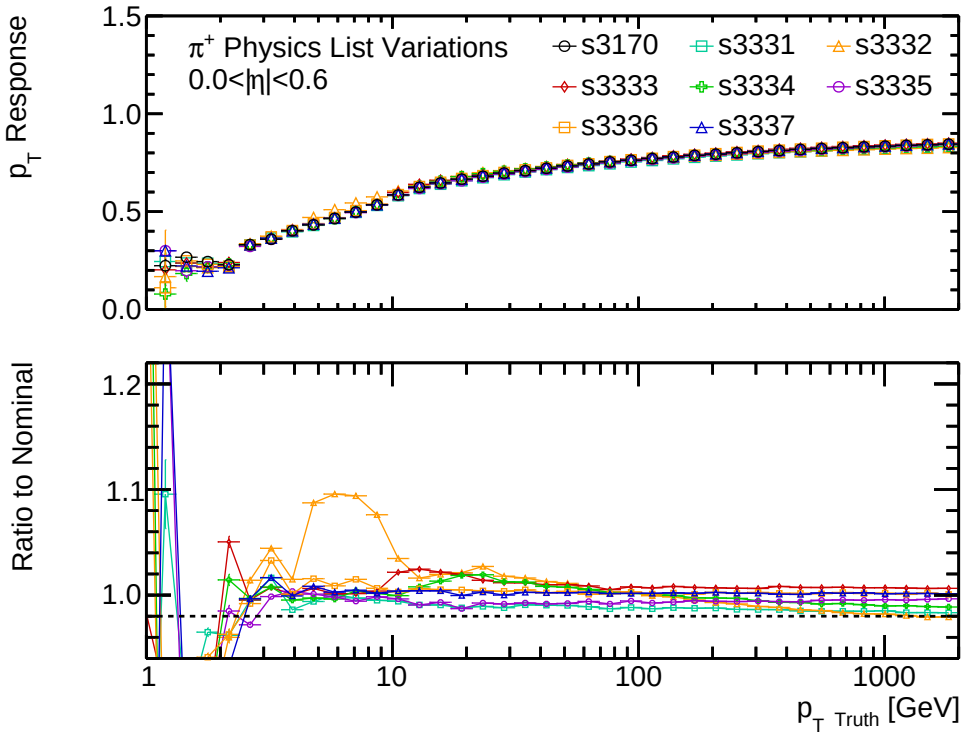

(a)

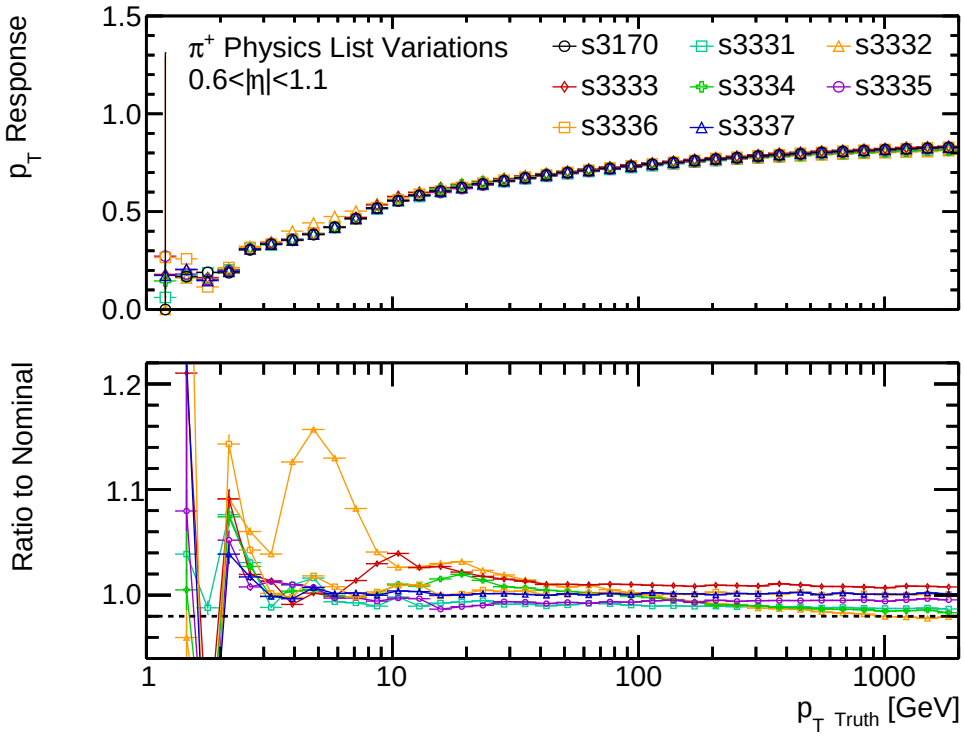

(b)

Figure 7.3: π^+ response and response ratio of different physics lists compared to the nominal as a function of truth p_T, sliced in $0.0< |\eta| <0.6$ (a) and $0.6< |\eta| <1.1$ (b). The physics list corresponding to each tag in the legend can be found in Table 4.1.

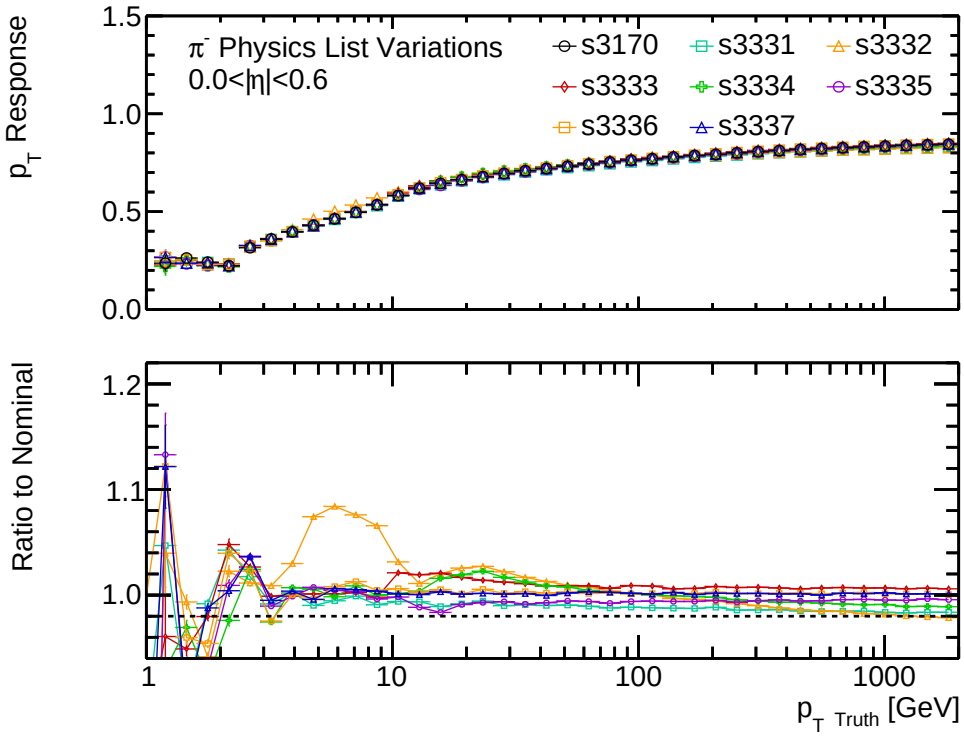

(a)

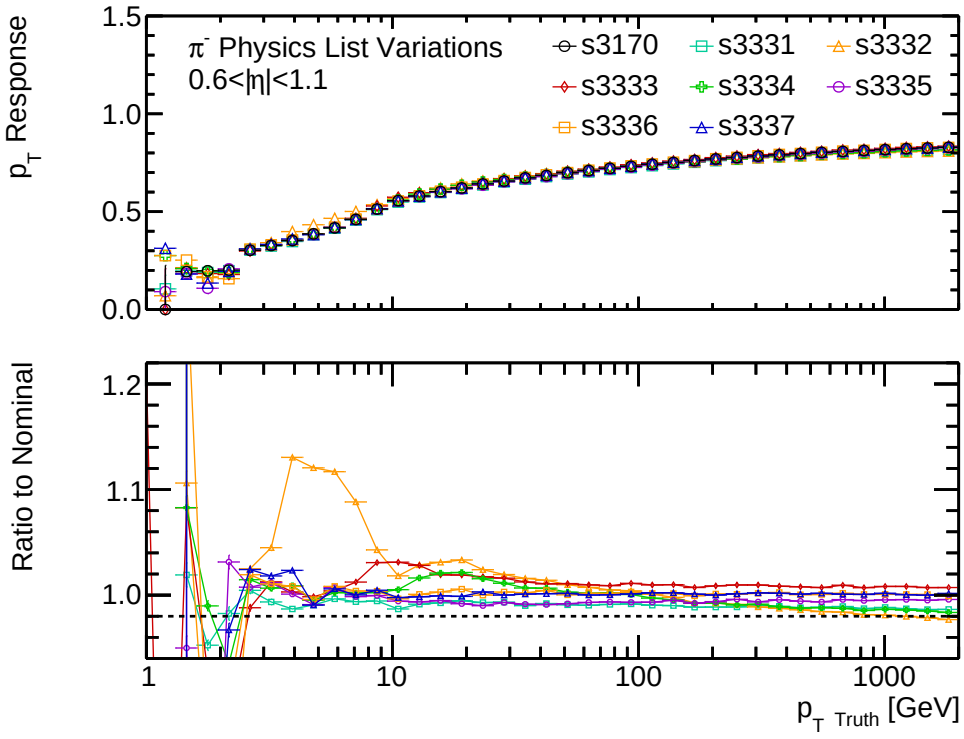

(b)

Figure 7.4: π^- response and response ratio of different physics lists compared to the nominal as a function of truth p_T, sliced in $0.0< |\eta| <0.6$ (a) and $0.6< |\eta| <1.1$ (b). The physics list corresponding to each tag in the legend can be found in Table 4.1.

7.2 Geometry List Variations

From Table 4.2 we know that geometry list `ATLAS-R2-2016-01-00-14` (s3369) includes additional material between the electromagnetic calorimeter and the hadronic calorimeter. As seen in the response ratio of Figure 7.5, this correlates to a < 1 ratio below η=1, a behavior which does not follow the other three geometry list variations. From Table 4.2 we also know that geometry list `ATLAS-R2-2016-01-00-15` (s3370) uses a distorted geometry of the detector components between the center of the detector and the electromagnetic calorimeter. As seen in the response ratio of Figure 7.5 this correlates to large deviations in the gap regions of the detector at η=1.5. This deviation is also different from the other three geometry list variations.

Note that the plots in Figure 7.5 only show the response for the 102.5-125.0 p_T slice, whilst in total there are 50 plots increasing in p_T and size logarithmically from 0.1-2000 GeV. By looking at all of these plots by eye, it was concluded that all response plots above 17.2 GeV show similar behavior to that shown in Figure 7.5. As shown in Figure 7.6, response plots below 17.2 GeV have large fluctuations, and the general behavior of the different geometry lists seen in the higher p_T slices is not as distinct. Again, these fluctuations are due to fit instability, which for the geometry list variations is discussed further in Appendix A.2..

Further work could be done to improve this, but as explained for the fluctuations of low p_T bins in Figure 7.2, 7.3, and 7.4, these fluctuations are not a major concern. Furthermore, it is important to note that since these are the results for pions, they will not be used to directly suggest a new K_L^0 uncertainty.

By comparing Figure 7.2, 7.3, and 7.4, we conclude that K_L^0 and pions behave similarly enough in terms of hadronic model variations that we can use the pion geometry variations in Figure 7.5 to support a generation request of K_L^0 MC samples to investigate the geometry lists `ATLAS-R2-2016-01-00-14` and `ATLAS-R2-2016-01-00-15`. These K_L^0 geometry samples will be used in future investigations to complement these studies for additional uncertainty components.

7.3 K_L^0 Uncertainty

Before suggesting a new single K_L^0 response uncertainty based on the results in Figure 7.2, it is important to note that `QGSP_BIC_HP_EMY` was constructed to be a worst case scenario physics list with the most possible differences to the nominal [45]. When investigating physics list variations, one should either use `QGSP_BIC_HP_EMY` as a single variation for a simplistic comparison, or use the full set of other variations [45]. However, due to problems in the MC sample generation, the list of variations used in this thesis is missing `FTFP_BERT_ATL_newElastic` [45]. The uncertainty contribution from `FTFP_BERT_ATL_newElastic` is not expected to be large, but to give a conservative suggestion for the K_L^0 response uncertainty we will therefore suggest it based on the envelope of the `QGSP_BIC_HP_EMY` response ratio. Using the envelope with maximum deviation from the nominal, the response ratio in Figure 1b is used to derive the new improved single K_L^0 response uncertainty. This new response uncertainty corresponds to 20% for $p_T <$ 10 GeV, 10% for 10 $< p_T <$ 100 GeV, 2% for p_T above 100 GeV

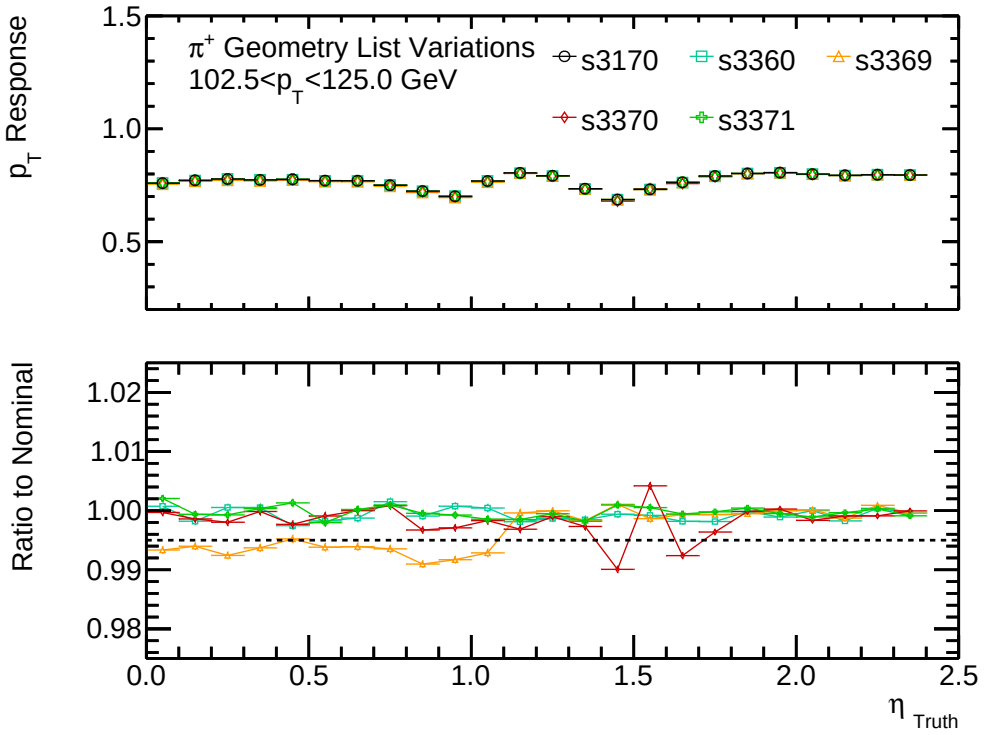

(a)

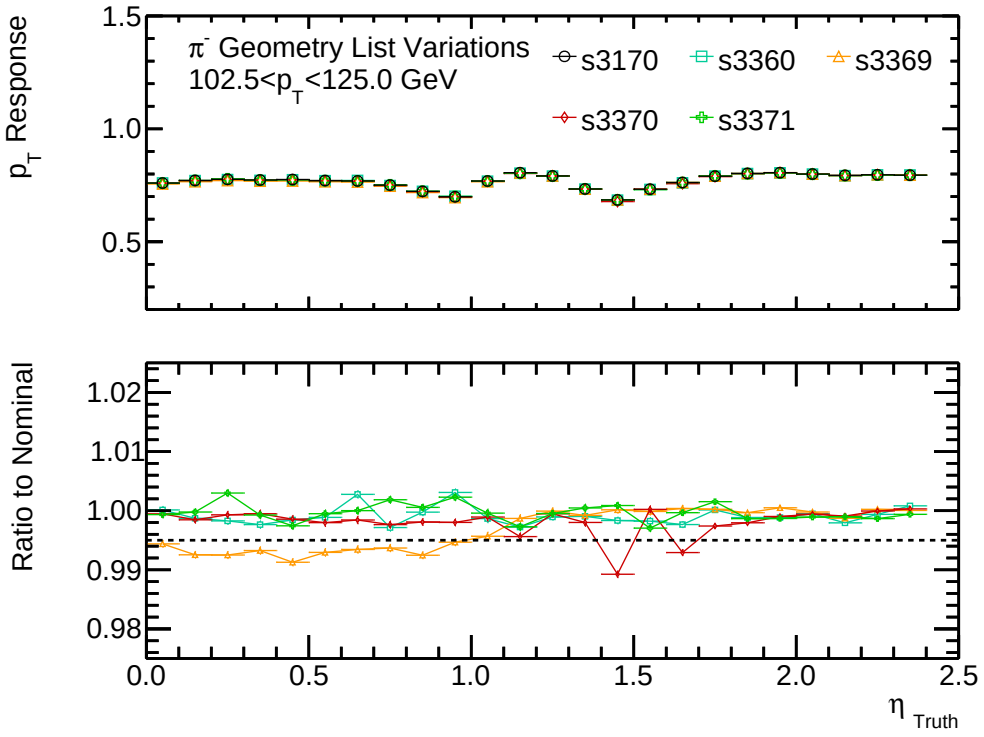

(b)

Figure 7.5: π^+ (a) and π^- (b) response and response ratio of different geometry lists compared to the nominal as a function of truth $|\eta|$, sliced in 102.5<p_T<125.0. The geometry corresponding to each tag in the legend can be found in Table 4.2.

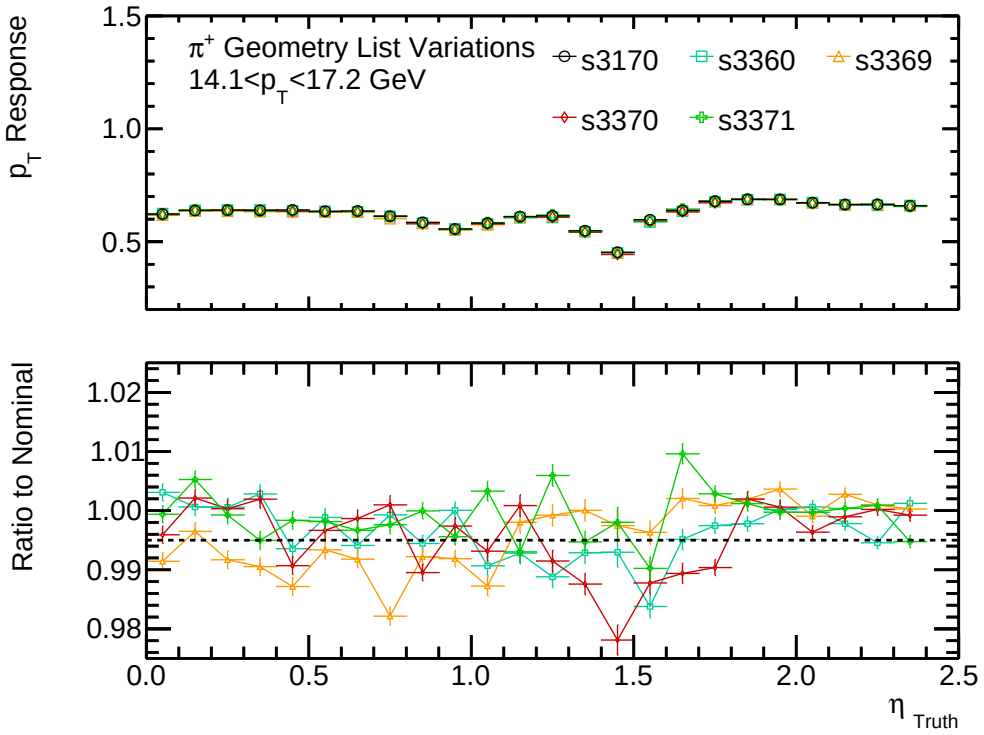

(a)

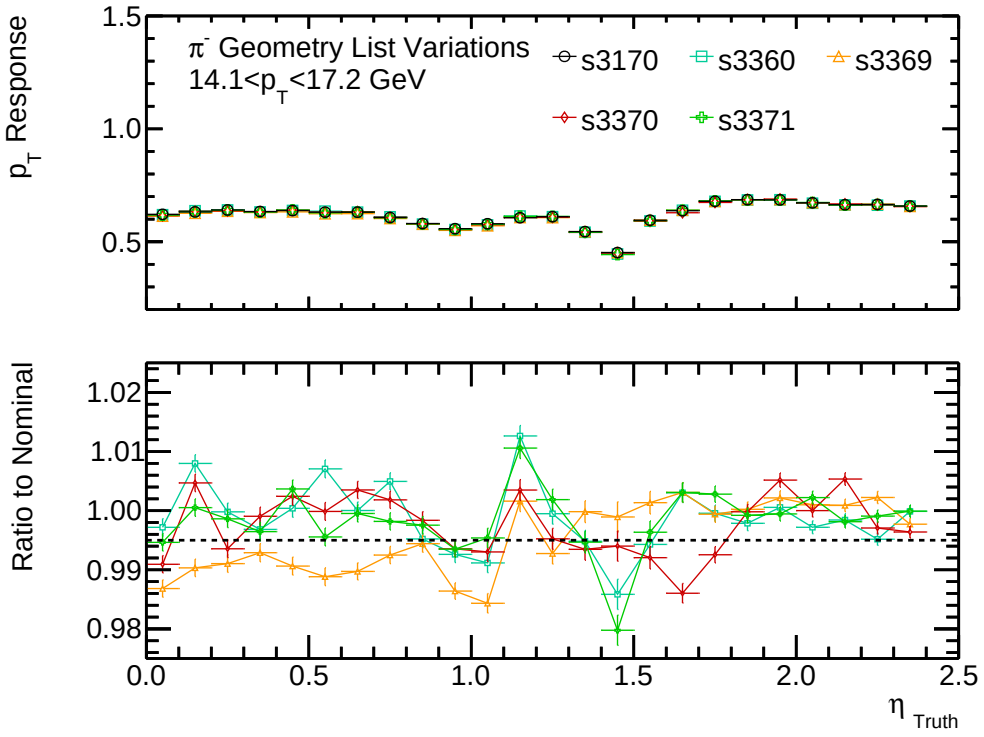

(b)

Figure 7.6: π^+ (a) and π^- (b) response and response ratio of different geometry lists compared to the nominal as a function of truth $|\eta|$, sliced in 14.1.5<p_T<17.2. The geometry corresponding to each tag in the legend can be found in Table 4.2.

Chapter 8

Conclusion and Outlook

Many analyses of ATLAS data are dependent on the jet energy scale (JES) calibration to correct the energy of the jets that are reconstructed in the detector, to that of the initial particles from the collision prior to detector effects. In simulation, the ratio of the reconstructed jet energy to the energy of these initial particles is called the jet energy response. The first aim of this thesis has been to develop the tools necessary to closely investigate the jet response after each of the different steps in the JES calibration, tools that can be used for these studies in the future.

Jet-based analyses are also dependent on the JES calibration uncertainty, and a major contribution to this comes from the uncertainty on the poorly known behavior of K_L^0. The main aim of this thesis is therefore to use the tools developed to derive a new improved K_L^0 uncertainty. This is done by evaluating the K_L^0 response for different physics lists, where a physics list is a collection of interaction models, and comparing them to the response of the physics list used to derive the calibration, called the nominal.

As a result, this thesis answers the question: "How much do the assumptions on the interactions undergone by the particles in the calorimeter affect the jet responses?". I have presented the reconstructed K_L^0 p_T responses for different physics lists as a function of generated truth particle p_T , in different slices of detector pseudorapidity η, and compared them to the K_L^0 response when using the nominal physics list. Information about the model specific details of these different physics lists has also been correlated to the features observed in the results.

Another question that is relevant for the K_L^0 uncertainty is: "Does the imperfect modeling of the ATLAS geometry in the simulations affect the K_L^0 response?". However, K_L^0 samples with different detector geometries simulated were not available. For this question, the similar behavior of the K_L^0 and pion responses when testing different physics lists allow us to assume that the K_L^0 p_T response for different geometries with respect to the nominal should be similar to that of the pions. With this assumption, one can use the generated samples with geometry list variations for the pions and propose to only generate the most deviating geometry lists as K_L^0 Monte Carlo (MC) samples for future K_L^0 uncertainty investigations. In any case, the response deviations from the geometry variations are negligible with respect to those from the physics lists, so we can derive a preliminary uncertainty by considering the largest response deviations from the physics list. The K_L^0 response and response ratio presented in this thesis are then used to derive a new improved K_L^0 response uncertainty of 20% for $p_T < 10$ GeV, 10% for 10 <pT< 100

GeV, 2% for p_T above 100 GeV.

In future work, the Trigger-object Level Analysis (TLA) will use the tools developed in this thesis to generate different response plots in order to confirm that the response after each step in the JES calibration is smooth, thereby decreasing the risk of the calibration inducing signal-like features in future analyses. The tools developed for this thesis can also be used in the near future with the newly generated K_L^0 geometry lists to further improve and/or better motivate the derived uncertainty. Lastly, the derived K_L^0 uncertainty presented in this thesis should be used in future analyses using K_L^0 responses, and it will be included in the upcoming estimation of the JES uncertainty.

Acknowledgements

First and foremost I want to thank Caterina Doglioni for being such a role-model supervisor. Some say that a great supervisor is one that is able to devise a project which is both meaningful for the scientific community and doable by a student. Not only have you managed to do both, but along the way you have always put my well-being, learning, and future career firsthand. Thank you for the opportunity to do such an amazing project with you and thank you for the many lessons learned. Nothing will have an impact on my life quite like this.

Thank you Will Kalderon for always being there to help and keep the project moving forward. Thank you for always replying and helping me out, it did not matter if it was in the early morning or late at night, whether it was a question about ROOT or where everyone went for lunch.

It is unlikely that this project would have turned out to be about the K_L^0 and have such potential as it does if it was not for Christopher Young's brilliant mind and dedication. Thank you for spending both time and effort in order to make this project into what it turned out to be.

Without Eric Corrigan, the code developed for this project would not be as elegant, functional, and maintainable as it is. You had a big role in this project and it would not have turned out as well as it did without you.

Getting a master's degree is difficult in many ways, but it is a lot easier if you share the burden. Therefore, I want to thank Emelie Olsson for always being such great classmate and colleague. Thank you for all the help and for all the laughs.

During her time as a guest professor at our division, Melissa Franklin left a huge impact on me. Thank you for the career advise, the stories, the weekly seminars, and thank you for teaching me that brutal honesty is something that should be valued.

Lastly, I want to thank my wonderful family Anders, Marita, and Matilda Ekman for always being such great sources of support, inspiration, and wise words. I want to thank you for helping me get to where I am today, it is truly a dream come true and none of this would have been possible without you.

References

[1] The Standard Model (2012). URL http://cds.cern.ch/record/1997201.

[2] Wikimedia Commons. File: Standard Model of Elementary Particles.svg — wikimedia commons, the free media repository (2019). URL https://commons.wikimedia.org/w/index.php?title=File:Standard_Model_of_Elementary_Particles.svg&oldid=341423479. [Online; accessed 8-June-2019].

[3] Martin, B. & Shaw, G. *Particle Physics*. Manchester Physics Series (Wiley, 2008).

[4] Kane, G. *Modern Elementary Particle Physics: Explaining and Extending the Standard Model* (Cambridge University Press, 2017).

[5] Thomson, M. *Modern particle physics* (Cambridge University Press, New York, 2013).

[6] Wu, C. S., Ambler, E., Hayward, R. W., Hoppes, D. D. & Hudson, R. P. Experimental Test of Parity Conservation in Beta Decay. *Phys. Rev.* **105**, 1413–1414 (1957).

[7] The Particle Data Group Collaboration. STRANGE MESONS (S=1, C=B=0)(S=1, C=B=0)(S=1, C=B=0)(S=1, C=B=0). *Phys. Rev.* **D98** (2019).

[8] Murayama, H. Physics Beyond the Standard Model and Dark Matter. In *Les Houches Summer School - Session 86: Particle Physics and Cosmology: The Fabric of Spacetime Les Houches, France, July 31-August 25, 2006* (2007). arXiv:0704.2276.

[9] Planck Collaboration. Planck 2018 results. vi. cosmological parameters (2018). arXiv:1807.06209.

[10] Womersley, J. Beyond The Standard Model. *Symmetry* **volume 02, issue 01** (2005).

[11] The Super-Kamiokande Collaboration. Evidence for oscillation of atmospheric neutrinos. *Phys.Rev.Lett.81* (1998). arXiv:hep-ex/9807003.

[12] Hyper-Kamiokande. Neutrinos and Neutrino Oscillation URL http://www.hyper-k.org/en/neutrino.html.

[13] Jönsson, L. *Lectures in Particle physics* (2016).

[14] The ATLAS Collaboration. Observation of a new particle in the search for the Standard Model Higgs boson with the ATLAS detector at the LHC. *Phys. Lett.* **B716**, 1–29 (2012). arXiv:1207.7214.

[15] The ATLAS Collaboration. Measurements of Higgs boson production and couplings in diboson final states with the ATLAS detector at the LHC. *Phys. Lett.* **B726**, 88–119 (2013). [Erratum: Phys. Lett.B734,406(2014)], arXiv:1307.1427.

[16] Pequenao, J. Computer generated image of the whole ATLAS detector (2008). CERN-GE-0803012.

[17] Schott, M. & Dunford, M. Review of single vector boson production in pp collisions at $\sqrt{s} = 7$ TeV. *Eur. Phys. J. C* **74**, 60 p (2014). URL http://cds.cern.ch/record/1699952. Comments: 60 pages, 64 figures, For Eur. Phys. J. C, arXiv:1405.1160.

[18] Wikimedia Commons. File:pseudorapidity2.png — wikimedia commons, the free media repository (2017). URL https://commons.wikimedia.org/w/index.php?title=File:Pseudorapidity2.png&oldid=260066972. [Online; accessed 8-June-2019].

[19] Huegging, F. The atlas pixel detector. *IEEE Trans.Nucl.Sci.* **53** (2006). arXiv:physics/0412138.

[20] Marko Mikužon on behalf of the ATLAS SCT Collaboration. The ATLAS SemiConductor Tracker. *EEE NSS* (2003).

[21] V. A. Mitsou for the ATLAS TRT collaboration. The atlas transition radiation tracker (2003). arXiv:hep-ex/0311058.

[22] Puzo, P. ATLAS calorimetry. *Nucl. Instrum. Meth.* **A494**, 340–345 (2002).

[23] Wigmans, R. & Wigmans, R. *Calorimetry: Energy Measurement in Particle Physics*. International series of monographs on physics.

[24] ATLAS Collaboration. The ATLAS Experiment at the CERN Large Hadron Collider. *JINST* **3**, S08003 (2008).

[25] Pequenao, J. & Schaffner, P. How ATLAS detects particles: diagram of particle paths in the detector (2013). URL https://cds.cern.ch/record/1505342. CERN-EX-1301009.

[26] Zhang, J. ATLAS Data Acquisition (2010). URL http://cdsweb.cern.ch/record/1239011/files/ATL-DAQ-PROC-2010-005.pdf. ATL-DAQ-PROC-2010-005, ATL-COM-DAQ-2009-055.

[27] Stelzer, J. The ATLAS high level trigger configuration and steering: Experience with the first 7-TeV collision data. *J. Phys. Conf. Ser.* **331**, 022026 (2011).

[28] Statistical hadronization and thermalization. URL http://alicematters.web.cern.ch/sites/alicematters.web.cern.ch/files/images/AM%20May%202017/Partonshower_hadronization.png.

[29] The ATLAS Collaboration. Topological cell clustering in the atlas calorimeters and its performance in lhc run 1. *Eur. Phys. J.* **C77** (2017). arXiv:1603.02934.

[30] Cacciari, M., Salam, G. P. & Soyez, G. The anti-k_t jet clustering algorithm. *JHEP* **04**, 063 (2008). arXiv:0802.1189.

[31] PYTHIA 8. URL http://home.thep.lu.se/~torbjorn/pythia81php/Welcome.php.

[32] Collaboration, T. G. GEANT4: A Simulation toolkit. *Nucl. Instrum. Meth.* **A506**, 250–303 (2003). SLAC-PUB-9350,FERMILAB-PUB-03-339.

[33] The ATLAS Collaboration. Jet energy scale measurements and their systematic uncertainties in proton-proton collisions at $\sqrt{s} = 13$ TeV with the ATLAS detector. *Phys. Rev.* **D96**, 072002 (2017). arXiv:1703.09665.

[34] The ATLAS collaboration. Monte Carlo Calibration and Combination of In-situ Measurements of Jet Energy Scale, Jet Energy Resolution and Jet Mass in ATLAS (2015). ATLAS-CONF-2015-037.

[35] Cacciari, M., Salam, G. P. & Soyez, G. Fastjet user manual (for version 3.3.2) (2011). arXiv:1111.6097.

[36] The ATLAS Collaboration. Jet energy measurement with the ATLAS detector in proton-proton collisions at $\sqrt{s} = 7$ TeV. *Eur. Phys. J.* **C73**, 2304 (2013). arXiv:1112.6426.

[37] The ATLAS Collaboration. Jet energy measurement and its systematic uncertainty in proton-proton collisions at $\sqrt{s} = 7$ TeV with the ATLAS detector. *Eur. Phys. J.* **C75**, 17 (2015). arXiv:1406.0076.

[38] Eva Hansen. Private communication.

[39] The ATLAS Collaboration. A measurement of the calorimeter response to single hadrons and determination of the jet energy scale uncertainty using LHC Run-1 *pp*-collision data with the ATLAS detector. *Eur. Phys. J.* **C77**, 26 (2017). arXiv:1607.08842.

[40] The ATLAS Collaboration. Jet energy scale and uncertainties in 2015-2017 data and simulation . URL https://atlas.web.cern.ch/Atlas/GROUPS/PHYSICS/PLOTS/JETM-2018-006/.

[41] The Particle Data Group Collaboration. Review of Particle Physics. *Phys. Lett.* **B667**, 1–1340 (2008).

[42] ATLAS Athena Guide. URL https://atlassoftwaredocs.web.cern.ch/athena/.

[43] Brief Overview Of The Geant4 Physics Models. URL https://geant4.web.cern.ch/results/brief_overview_of_the_geant4_physics_models.

[44] Abat, E. *et al.* Response and shower topology of 2 to 180 GeV pions measured with the ATLAS barrel calorimeter at the CERN test-beam and comparison to Monte Carlo simulations (2010). ATL-CAL-PUB-2010-001.

[45] Dotti, A. Alternatives Physics Lists, ATLAS Report. URL https://indico.cern.ch/event/686200/contributions/2821576/attachments/1574475/2485739/ATLAS_Physics_Lists_Alternatives1.pdf.

[46] FTFP_BERT. URL http://geant4-userdoc.web.cern.ch/geant4-userdoc/UsersGuides/PhysicsListGuide/html/reference_PL/FTFP_BERT.html.

[47] Welcome to the Guide for Physics Lists! URL http://geant4-userdoc.web.cern.ch/geant4-userdoc/UsersGuides/PhysicsListGuide/html/index.html.

[48] The ATLAS Collaboration. Search for low-mass dijet resonances using trigger-level jets with the ATLAS detector in pp collisions at $\sqrt{s} = 13$ TeV. *Phys. Rev. Lett.* **121**, 081801 (2018). arXiv:1804.03496.

[49] ROOT Release 6.14/00 - 2018-06-13. URL https://root.cern.ch/content/release-61400.

[50] SimpleJetTriggerAlgos. URL https://gitlab.cern.ch/atlas-trigger/jet/SimpleJetTriggerAlgos.

[51] The Python Language Reference URL https://docs.python.org/2/reference/index.html.

[52] JES_ResponseFitter. URL https://gitlab.cern.ch/atlas-jetetmiss-jesjer/tools/JES_ResponseFitter/tree/master.

Appendix A

Low p_T Fit Fluctuations

A.1 p_T Response as a Function of p_T, sliced in $|\eta|$

This section discusses the fluctuation in p_T response seen in the low p_T bins of Figure 7.2, 7.3, and 7.4 of the K_L^0 physics list variations. This discussion will be based on looking at some individual fits of the K_L^0 nominal Monte Carlo (MC) sample. The fits were made using `JES_BalanceFitter.py` [52], which among other things, optimizes the binning of the histograms for the fit.

In Figure A.1a we see that the distribution of the 1D histogram from the 2.90-3.53 GeV p_T bin has a poor Gaussian shape which is asymmetric and has large tails. This bad shape is consistent for the histograms in the sub-10 GeV region and leads to fluctuations of the fit mean and therefore fluctuations of the responses in Figure 7.2, 7.3, and 7.4. For Figure A.1b and A.2a we see that the shape of the distribution improves with increasing p_T. In fact, the asymmetry of the histograms appear by construction: since the p_T of the truth particle cannot fluctuate below zero, as negative energy topo-clusters are not included in this analysis, the calorimeter response misses the downwards fluctuations and is skewed towards the upwards fluctuations. This also explains why the Gaussian shape of the response improves with p_T.

As discussed in Section 7.1.1, Figure 5.3 shows that above 2000 Gev the main hadronic contribution to the total jet energy comes from hadrons of $p_T > 350$ GeV. Since the K_L^0 response uncertainty extrapolation to the Jet Energy Scale (JES) uncertainty is not currently used below the 2415 GeV limit of the in-situ calibration, this means that bad fits are not a major concern for K_L^0 below 350 GeV. From Figure A.2b we see that for K_L^0 just below 350 GeV, it has a nice Gaussian distribution with a good fit. A behavior which is consistent for the higher p_T histograms.

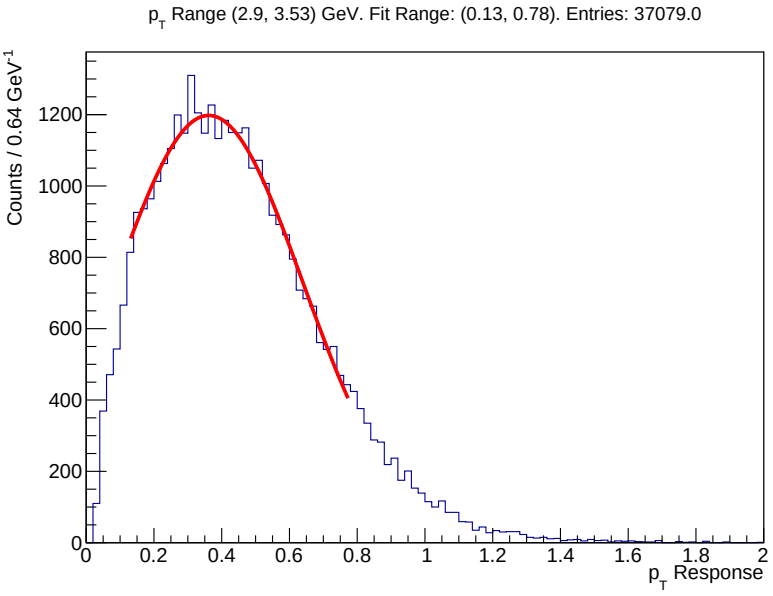

(a)

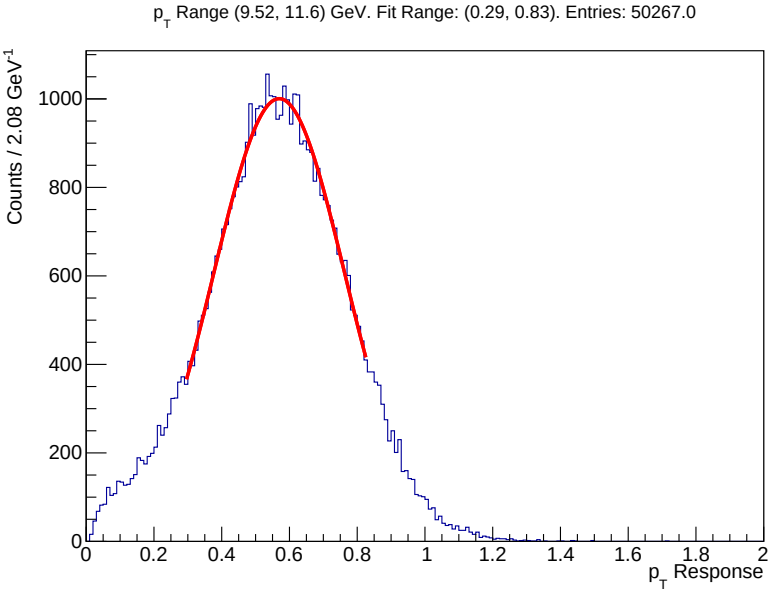

(b)

Figure A.1: The 1D histogram with a Gaussian fit of slice 0.0< $|\eta|$ <0.6 and p_T bin 2.90-3.53 GeV (a) and 9.52-11.60 GeV (b). The mean of the fit determines the response in the specific p_T bin, for that $|\eta|$ slice.

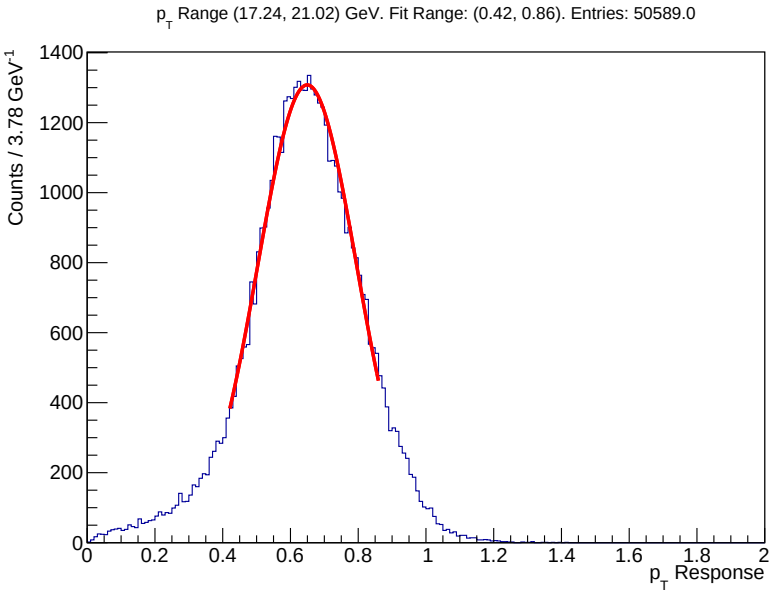

(a)

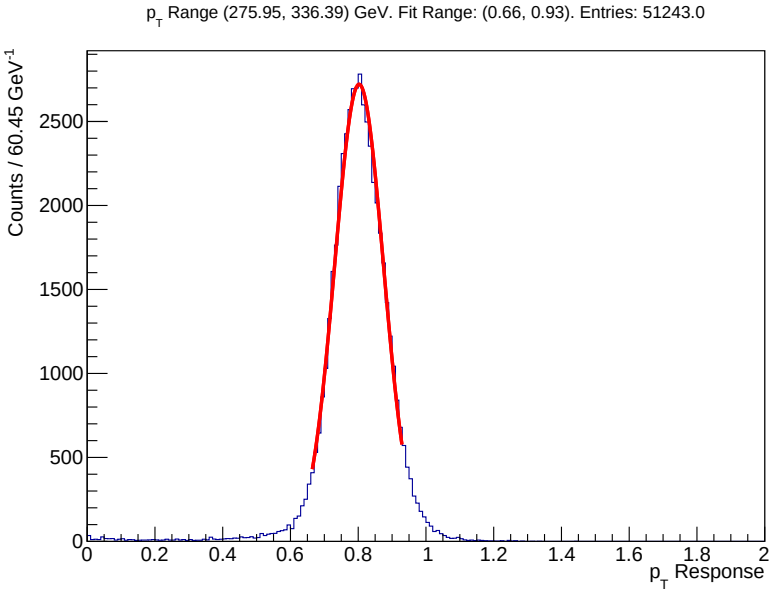

(b)

Figure A.2: The 1D histogram with a Gaussian fit of slice 0.0< $|\eta|$ <0.6 and p_T bin 17.24-21.02 GeV (a) and 275.95-336.39 GeV (b). The mean of the fit determines the response in the specific p_T bin, for that $|\eta|$ slice.

A.2 p_T Response as a Function $|\eta|$, sliced in p_T

This section discusses the increased fluctuation in response seen when comparing the high p_T slice of Figure 7.5 to the lower p_T slice of Figure 7.6 of the pion geometry variations. This discussion will be based on looking at some individual fits of the nominal π^+ MC sample.

As seen in Figure A.3, the distribution has the same asymmetric shape and long tails as the low p_T histogram covered in Section A.1. The reason for this asymmetry and its improvement with increasing pt, as seen in Figure A.4 and A.5, is the same as explained in Section A.1.

As discussed earlier in Section A.1 and 7.1.1, we are not concerned about poor fits far below 350 GeV. For this specific section, it is also important to note that this thesis does not take the pion responses into consideration when deriving the new K_L^0 response uncertainty. However, for good measure, as can be seen in figure A.5b, for the p_T slice just under 350 GeV, the histogram has a nice Gaussian distribution with a good fit. A behavior which again is consistent for the higher p_T histograms.

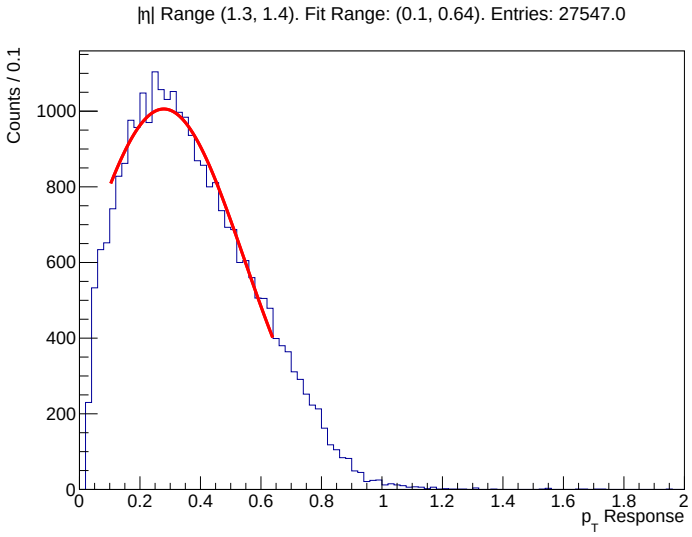

Figure A.3: The 1D histogram with a Gaussian fit of slice $2.90<p_T<3.53$ in $|\eta|$ bin 1.3-1.4. The mean of the fit determines the response in the specific $|\eta|$ bin, for that p_T slice.

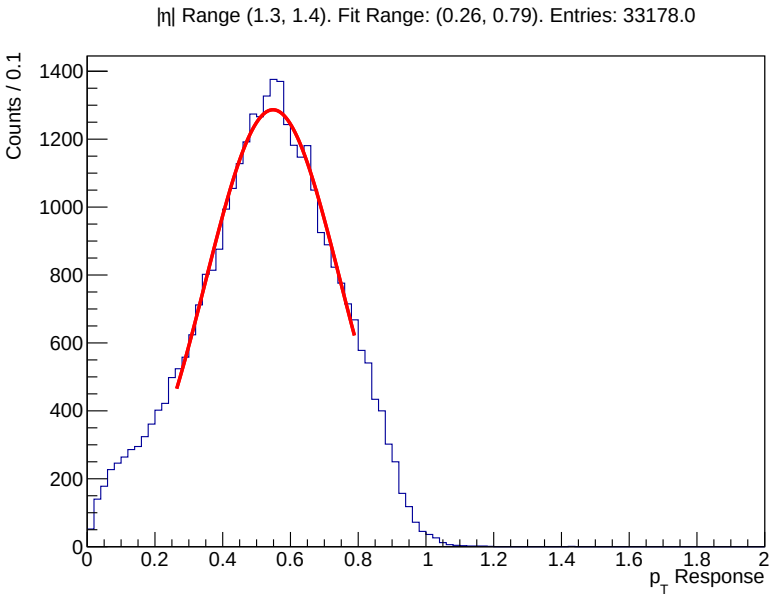

(a)

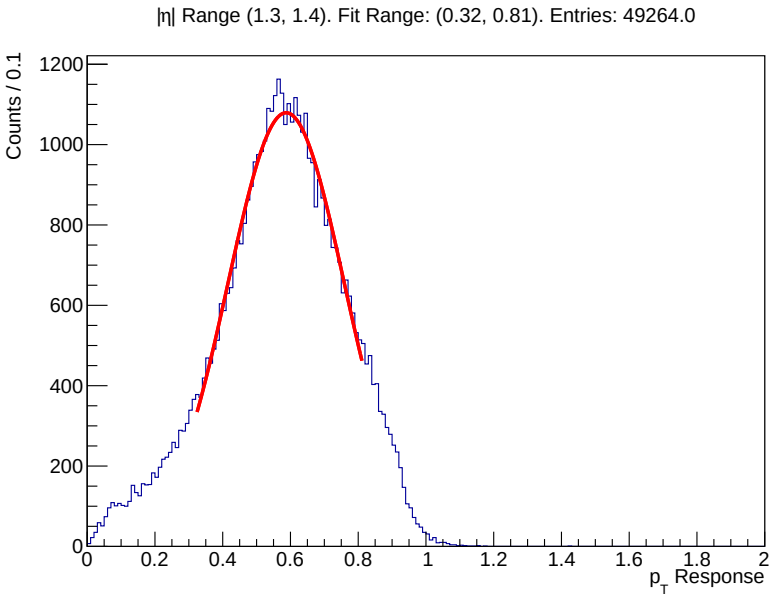

(b)

Figure A.4: The 1D histogram with a Gaussian fit of slice $14.14<p_T<17.24$ (a) and $17.24<p_T<21.01$ (b) in $|\eta|$ bin 1.3-1.4. The mean of the fit determines the response in the specific $|\eta|$ bin, for that p_T slice.

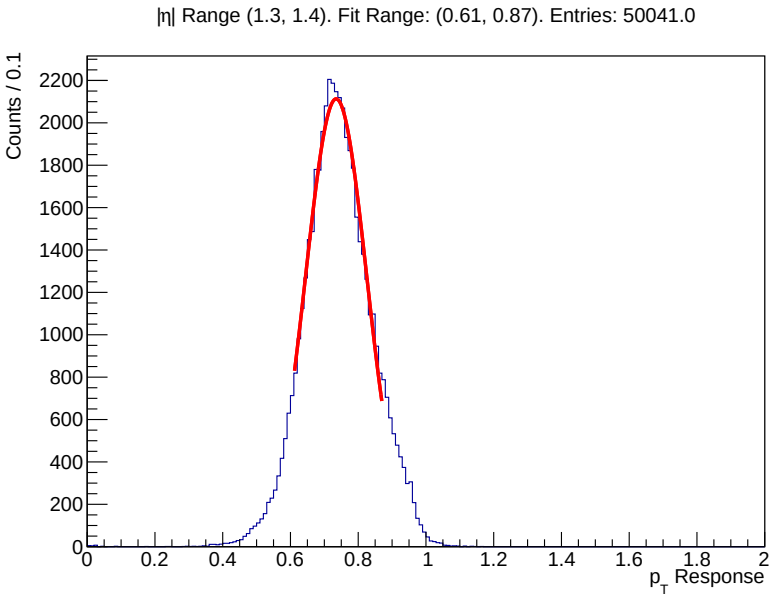

(a)

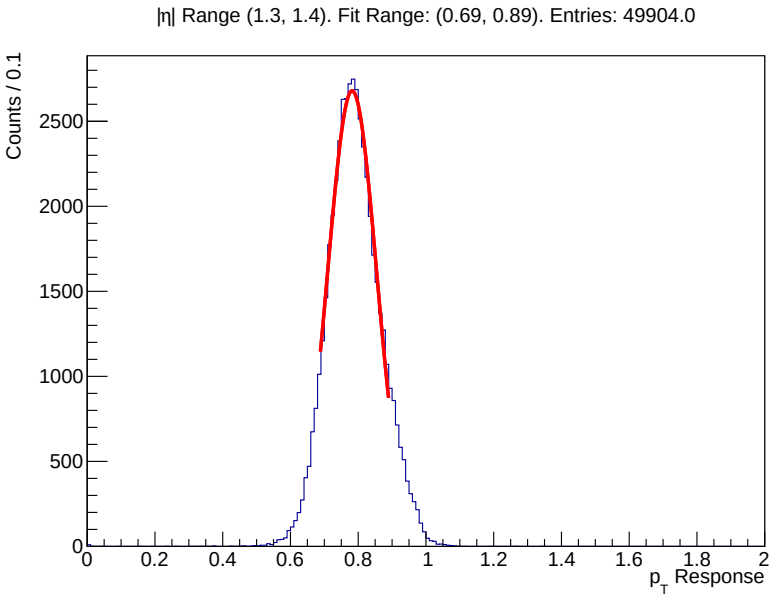

(b)

Figure A.5: The 1D histogram with a Gaussian fit of slice $102.50<p_T<125.00$ (a) and $275.95<p_T<336.39$ (b) in $|\eta|$ bin 1.3-1.4. The mean of the fit determines the response in the specific $|\eta|$ bin, for that p_T slice.